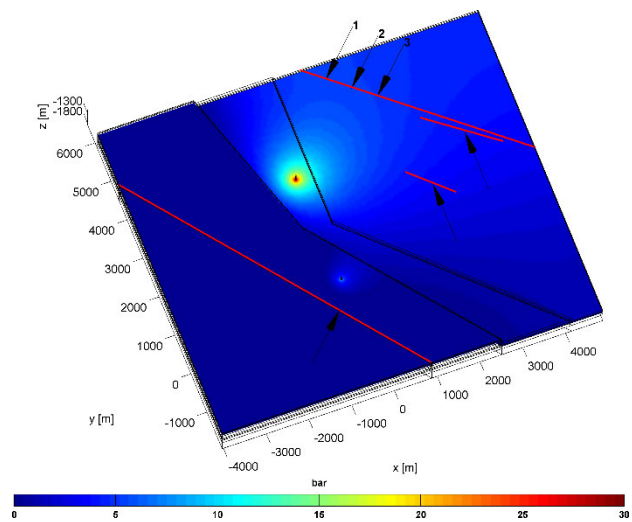


# Seismic Hazard Assessment for the CLG-Geothermal System – Study Update March 2019



**CLG006**

**COPYRIGHT** This report has been prepared for the internal use of CLG. The concepts and information contained in this document may not be published or given to third parties without written approval of Q-con GmbH.

**DISCLAIMER** Neither Q-con GmbH nor any person acting on behalf of Q-con GmbH:

- makes any warranty or representation, express or implied, with respect to the accuracy, completeness, or usefulness of the information contained in this report, or that the use of any apparatus, method, or process disclosed in this report may not infringe privately owned rights; or
- assumes any liability with respect to the use of, or for damages resulting from the use of, any information, apparatus, method, or process disclosed in this report.

Report title:	Seismic Hazard Assessment for the CLG-Geothermal System – Study Update March 2019
Author(s):	██████████, ██████████
Report date:	22 <sup>nd</sup> March 2019
Project:	Californie
Prepared for:	CLG
Version:	190322
Archive No.:	CLG006

**Contents**

**1 Background.....5**

**2 Scope of Study .....6**

**3 Overview.....7**

**4 Physical Mechanisms of Induced Seismicity .....8**

**5 Induced Seismicity Observations in other Geothermal Reservoirs .....11**

**6 Californië Geothermal Site .....15**

**6.1 Regional Geology..... 15**

**6.2 Natural Faults ..... 15**

**6.3 Stress Field..... 18**

**6.4 Stress State on Natural Faults ..... 21**

**6.5 Local Seismicity ..... 23**

**6.6 Geothermal Operations ..... 28**

**7 Californië Reservoir Model .....30**

**7.1 VITO Model..... 30**

**7.2 Model Implementation ..... 33**

**8 Seismic Hazard .....37**

**8.1 Hydraulic Overpressure..... 37**

**8.2 Thermal Reservoir Contraction..... 40**

**8.3 Hazard Assessment ..... 41**

        8.3.1 Seismicity Potential ..... 41

        8.3.2 Metric ..... 42

        8.3.3 Magnitude Thresholds ..... 43

        8.3.4 Mitigation Measures ..... 43

**8.4 Qualitative Risk Assessment ..... 44**

**9 Recommendations .....46**

**References .....47**

---

<b>Appendix A Seismic Station Network .....</b>	<b>51</b>
<b>Appendix B Additional Numerical Simulations .....</b>	<b>52</b>
<b>B.1. Fluid Pressure.....</b>	<b>52</b>
<b>B.2. Thermal Reservoir Contraction .....</b>	<b>55</b>

## 1 BACKGROUND

Two geothermal doublet systems have been operated at the Californië geothermal site near Venlo to supply greenhouses with heat. Both systems, operated by Californie Lipzig Gielen BV (CLG doublet GT04-GT05) and Californië Wijnen Geothermie (CWG doublet GT01-GT03), are located in close proximity with inter-wellbore distances in the order of a few kilometers only. Both doublet systems target the Carboniferous Limestone Group and fluid is produced from the Tegelen fault zone that intersects the reservoir formation. The CWG-doublet started operations in February 2014 and the CLG doublet commenced operational testing in September 2017.

On 03.09.2018 18:20:31 UTC, a felt  $M_L=1.7$  earthquake occurred near the Californië geothermal site. In the same region, several small magnitude events ( $M_L=-1.2$  to  $M_L=0.3$ ) were observed previously over the last years. The felt earthquake occurred after both geothermal systems have stopped operations, the CWG system already in May 2018 and the CLG system 6 days prior to the felt earthquake. As of February 2019, neither of the two geothermal doublets at Californië has resumed geothermal production.

The seismicity and the underlying geomechanical processes were investigated in a subsequent study (Baisch & Vörös, 2019). Thermal reservoir contraction at the CWG injection well was identified as the most likely mechanism causing the seismicity at the Californië site, while the timing of the earthquakes is influenced by production-related pressure drawdown in the Tegelen fault.

### 2 SCOPE OF STUDY

The previous seismic hazard assessment (Vörös et. al, 2015) shall be updated taking into account the observed seismicity and its interpretation (Baisch & Vörös, 2019). The updated study shall provide a basis for deciding if the CLG doublet can resume geothermal production in a safe and responsible way. For the current study it shall be assumed that the CWG doublet will not resume operations.

## 3 OVERVIEW

The seismic hazard assessment conducted in the current study is based on a deterministic analysis of the stress changes associated with geothermal production.

For this, the basic geomechanical processes that could lead to induced seismicity are discussed in chapter 4 and observations from a global data set outlining general characteristics of the induced seismicity are presented in chapter 5.

Chapter 6 summarizes the subsurface conditions at the Californië geothermal site, the previous geothermal operations and the observed seismicity. A local reservoir model and its numerical implementation are described in chapter 7.

The seismic hazard for a future production scenario is assessed in chapter 8. Hydraulic overpressure and thermal reservoir contraction are identified as the relevant sources causing stress changes. Using numerical simulations it is demonstrated that the stress changes associated with a future 20 years CLG production scenario are extremely small on the known faults. It is concluded that resuming geothermal production with the CLG doublet will most likely not cause seismicity on the known faults. Acknowledging uncertainties of subsurface conditions, a traffic light system is proposed for limiting the strength of earthquakes potentially occurring on an unmapped fault. With the proposed TLS, the remaining seismic risk associated with resuming CLG production is considered to be acceptable.

It is, however, recommended to review the concept and assumptions of the current study in case any seismic event (regardless of magnitude) occurs during future production of the CLG doublet (chapter 9). In particular we recommend stopping production if an earthquake occurs in the vicinity of the previous cluster of seismic activity near the CWG injector. Such an earthquake could indicate that earthquakes can be triggered at a lower stress perturbation level than considered in the current study.

## 4 PHYSICAL MECHANISMS OF INDUCED SEISMICITY

The phenomenon of man-made seismicity is known from different energy technologies such as mining, oil and gas exploitation, water impoundment and from geothermal reservoirs (National Academy of Science, 2013). The physical mechanisms underlying the induced seismicity are controlled by stress changes in the subsurface caused by anthropogenic activities.

If stress changes act on a pre-existing fracture or similar zone of weakness, seismicity may occur on the fracture if the ratio between shear- and effective normal stress exceeds the coefficient of friction. Let  $\tau$  and  $\sigma_n$  denote the shear and normal stresses resolved on a fracture plane,  $p_n$  the *in situ* fluid pressure, and  $\mu$  the coefficient of friction, then shear slippage occurs on the fracture if (e.g. Healy et al., 1970; Hsieh and Bredehoeft, 1981):

$$\text{Equation 1:} \quad \tau / (\sigma_n - p_n) > \mu$$

assuming zero cohesion.

Stress perturbations can be described by Coulomb stress changes  $\Delta CS$ , which are defined as (e.g. Scholz, 2002)

$$\text{Equation 2:} \quad \Delta CS = \Delta \tau - \mu \cdot (\Delta \sigma_n - \Delta p_n),$$

reflecting the condition for criticality according to Equation 1. Positive values of Coulomb stress changes increase, negative values decrease the tendency to failure on a fault.

Mechanisms causing seismicity in geothermal reservoirs include

- fluid pressure increase due to fluid injection,
- thermally induced stresses (thermal reservoir contraction),
- mass changes,
- poroelastic stress changes,
- and chemical processes.

All of these mechanisms may be relevant for a certain type of geothermal operation. It is noted, however, that the strongest seismic events observed to date in geothermal reservoirs are interpreted as being caused by fluid overpressure.

The occurrence of perceptible induced seismicity requires several conditions:

1. Shear-stresses need to be resolved on an existing shearing plane in the subsurface, e.g. a critically stressed fault.
2. The shearing plane needs to be mechanically strong enough to support high shear-stresses, implying a significant strength of the associated rocks. Seismic energy is only released if the hardness of the rocks is sufficiently large to allow for an almost instantaneous failure. Sedimentary rocks usually exhibit a smaller strength compared to crystalline rock (e.g. Abdullah, 2006). This could explain why (noticeable) injection induced seismicity typically occurs in the crystalline basement (e.g. Evans et al., 2011).



3. The dimensions of the critically stressed fault need to be large enough to host a perceptible earthquake.

In general, the strength of an induced earthquake is controlled by the dimension of the shearing plane:

*Equation 3:* 
$$M_0 = G A d,$$

where  $M_0$  is the seismic moment,  $G$  denotes shearing modulus,  $A$  is the area of the shearing plane, and  $d$  is the average slip occurring on the shearing plane. Simple mechanical considerations reveal that the shear slip displacement  $d$  cannot become arbitrary large, but is limited by (1) the capacity of the surrounding rock to absorb deformation, and (2) by the amount of shear stress driving the failure process. Therefore, the dominating parameter controlling the strength of an induced event is the area  $A$  of the associated shearing plane.

Several empirical relationships exist to convert seismic moment to earthquake magnitude. Following Hanks & Kanamori (1979), we use

*Equation 4:* 
$$M_w = 2/3 \cdot \log(M_0) - 6.1$$

for the determination of the moment magnitude  $M_w$ . This moment magnitude scale is also used by the Royal Netherlands Meteorological Institute (KNMI), e.g. to determine earthquake strength of seismicity in the Groningen gas field. The standard magnitude scale used by KNMI, however, is a local magnitude  $M_L$  as defined in Dost et al. (2004), and later replaced by the  $M_L$  definition of Akkar et al. (2013).

In principle, the strength of an induced earthquake can be estimated based on the fault area on which Coulomb stress changes  $\Delta CS$  cause overcritical stress conditions. This, however, requires an assumption on the fault's virgin stress-strength conditions, which are generally not known.

For seismicity induced by fluid injections into the geothermal reservoir at Soultz-sous-Forêts, Baria et al. (2004) estimate that seismicity is triggered by hydraulic overpressure exceeding 3 MPa, which is consistent with numerical simulations of hydraulic overpressure in other EGS reservoirs (e.g. Cooper Basin, Baisch et al., 2015). A global lower bound value for a fluid pressure triggering threshold, however, does not exist as the lower bound value is location- and time-dependent and can become arbitrarily small during the nucleation process of tectonic earthquakes.

Fluid pressure triggering threshold values as low as 0.01 MPa have been discussed in the scientific literature (see overview paper by Costain & Bollinger, 2010). E.g. Keranen et al. (2014) conclude that wastewater injection into the Arbuckle formation causes seismicity at an overpressure level as small as 0.07 MPa. Their conclusion is based on a numerical model where fluid diffusion exhibits homogeneous, three-dimensional characteristics (Figure 4 of Keranen et al., 2014). Alternative models with a connected set of fractures, however, provide more efficient pressure propagation, resulting in a higher level of overpressure required for earthquake triggering. For example, Schoenball et al. (2018) estimate the triggering pressure

for Oklahoma seismicity to be in the order of 0.2-0.8 MPa.

A similar situation is reflected in the discussion of Husen et al. (2007) and Miller (2008). Husen et al. (2007) assume a numerical model with matrix diffusion to estimate a level of 100 Pa fluid overpressure at which earthquakes are triggered by rainfall. Using the same data, Miller (2008) estimates a triggering level in the order of 1 MPa when accounting for the strongly carstified rock.

In principle, stress perturbations, such as dynamic stresses associated with passing waves from natural earthquakes place a lower limit to the triggering threshold. These stress perturbations can be as large as 1 MPa (Hill, 2008), but are depending on geometrical details of the receiver fault and therefore do not define a strict lower limit.

## 5 INDUCED SEISMICITY OBSERVATIONS IN OTHER GEOTHERMAL RESERVOIRS

As outlined in the previous section, different mechanisms may induce seismicity in geothermal reservoirs, while the dominating mechanism is elevated pore pressure. There exist, however, only few documented cases of induced seismicity occurring during mass balanced geothermal circulations. Case histories include the geothermal system at Unterhaching (Germany), where a maximum magnitude of  $M_L=2.4$  occurred (Megies & Wassermann, 2014) as well as the geothermal system at Landau (Germany) with a maximum event magnitude of  $M_L=2.7$  (Bönnemann et al., 2010) and the Insheim (Germany) system with a maximum event magnitude of  $M_L=2.4$  (Küperkoch et al., 2018). In these systems, noticeable seismicity occurred after several years of operating the geothermal system.

For example, Figure 1 compares activities at the geothermal site at Insheim (Germany) to earthquake occurrence. The geothermal system at Insheim directly targets an active Graben structure (Rhine Graben) at the intersection between sedimentary cover and crystalline basement. Geothermal operations at Insheim are accompanied by pronounced seismic activity, some of which is correlated to stopping and re-starting production. For example, immediately after a pump failure in 2013 (purple shaded area in Figure 1), a felt  $M_L=1.9$  earthquake occurred which, at that time, was the strongest earthquake observed at Insheim. Most notably, the maximum earthquake strength has not changed very much in the time period 2012 to 2018.

Larger data sets of induced seismicity exist in the context of hydraulic stimulations. Although the current study focusses on seismicity occurring during geothermal production, typical characteristics of seismicity related to the general context of fluid injection (also applying to re-injecting fluid during geothermal production) can be studied using observations from hydraulic stimulations.

In granitic reservoirs, hydraulic stimulations typically produce large amounts of induced earthquakes, the largest of which exhibit magnitudes in the order of  $M_L=3.5$  (Evans et al., 2011). In sedimentary reservoirs, induced seismicity is less common and even massive hydraulic stimulations typically do not produce noticeable seismicity (e.g. Bunes, 2004; Kwiatek et al., 2010).

Typical observations of geothermal reservoir seismicity include:

- The Kaiser-Effect, implying that induced seismicity occurs only at those locations in a reservoir, where previously experienced *in situ* fluid pressures are exceeded (e.g. Baisch et al., 2009). The Kaiser-Effect follows directly from the Mohr-Coulomb failure criterion (Baisch & Harjes, 2003).
- A systematic (temporal) increase of the maximum magnitude of the induced seismicity (Figure 2). This characteristic forms the basis for implementing a 'Traffic Light System' for risk mitigation (Bommer et al., 2006).
- The occurrence of seismic activity after a hydraulic stimulation has been terminated (post-injection seismicity, 'trailing effect'), with the largest magnitude event frequently

occurring after shut-in (Baisch et al., 2006; 2010). Figure 3 shows data examples of geothermal activities and related seismicity response. In these examples, the largest trailing effect was observed after the stimulation of the DHM geothermal reservoir at Basel (Switzerland) and corresponds to a post-injection magnitude increase of 0.8  $M_L$  magnitude units. It is currently discussed if the  $M_w$ 5.4 earthquake at Pohang (Kim et al., 2017) was triggered by geothermal stimulations, implying a possible trailing effect in the order of 2 magnitude units.

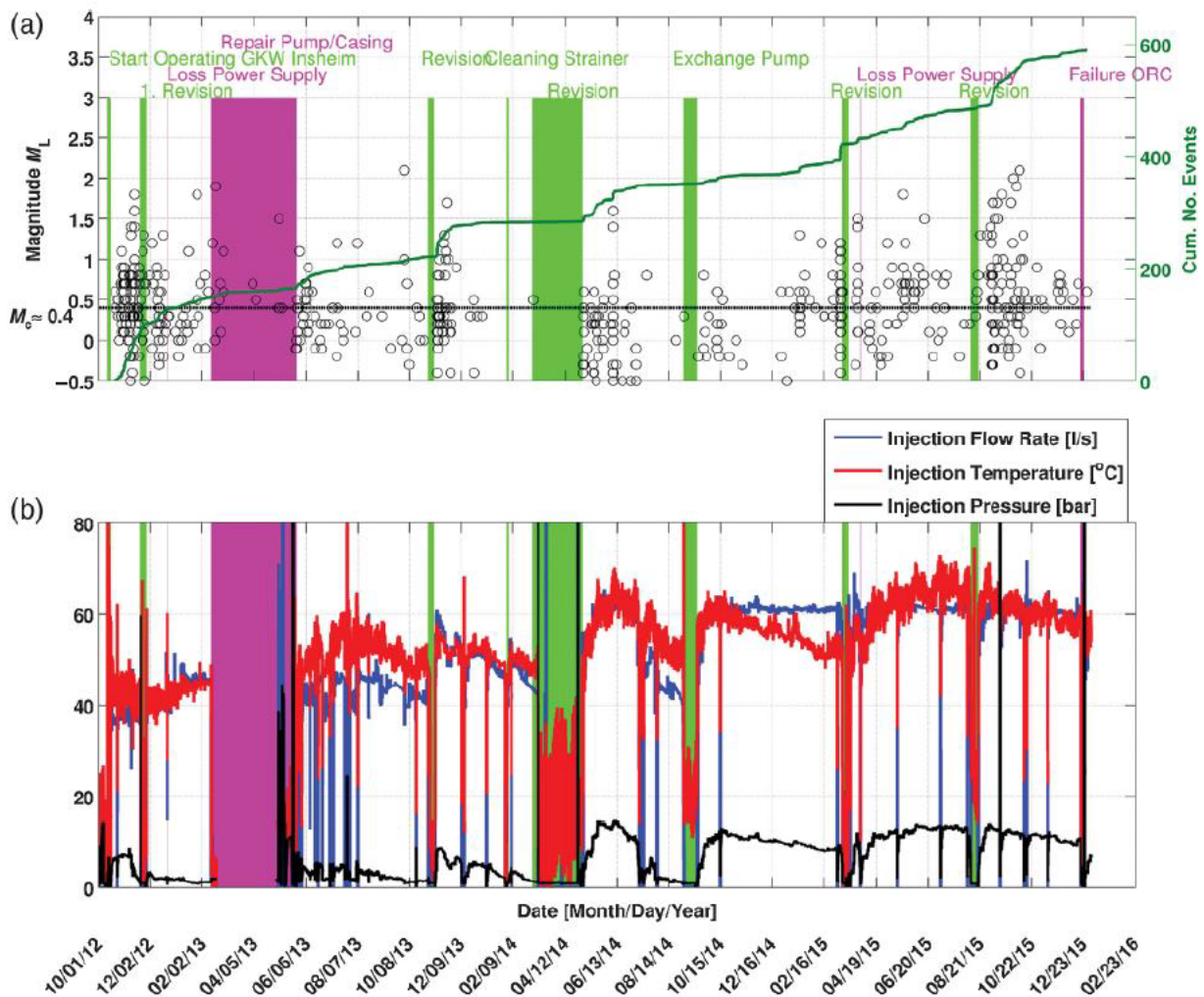


Figure 1: Geothermal activities compared to earthquake occurrence at Insheim (Germany). Earthquake activity (and earthquake strength) frequently increase shortly after production stop (colored shading). Figure from Küperkoch et al. (2018).

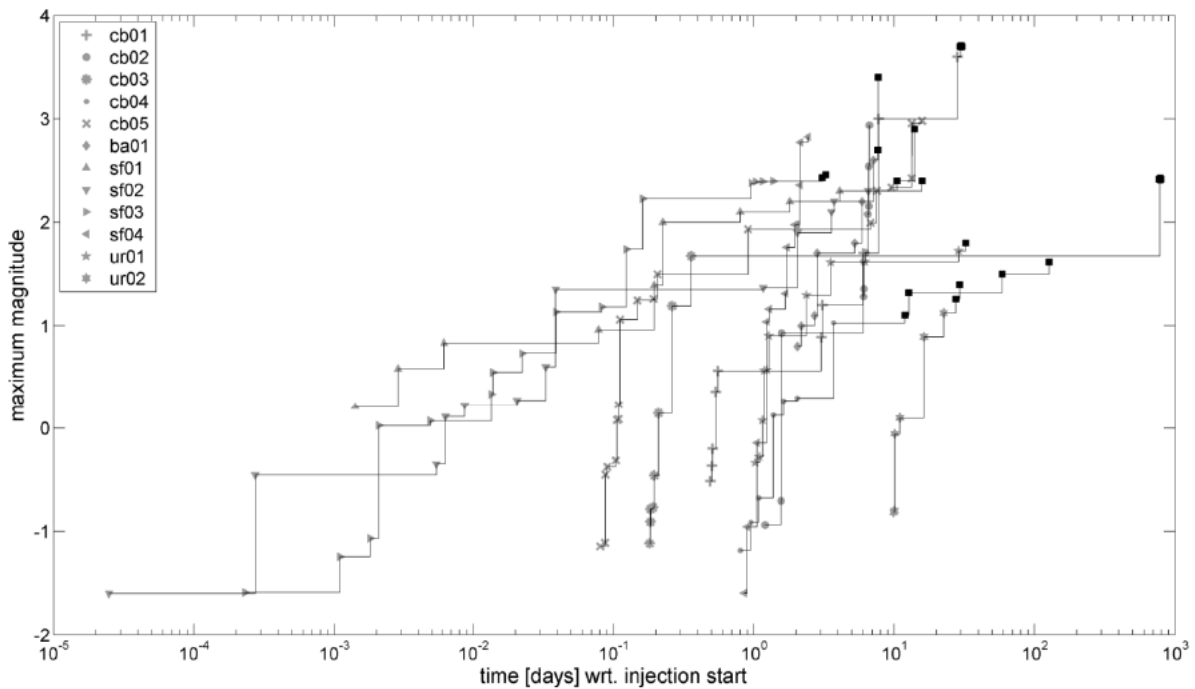


Figure 2: Maximum event magnitude as a function of injection time during hydraulic stimulation at different geothermal sites (cb Cooper Basin; ba Basel; sf Soultz-sous-Forets; ur Bad Urach). Note that data points are generated whenever previous maximum magnitudes are exceeded. Thus, a large number of data points indicate a gradual increase of the maximum event magnitude. Figure from Baisch et al. (2019).

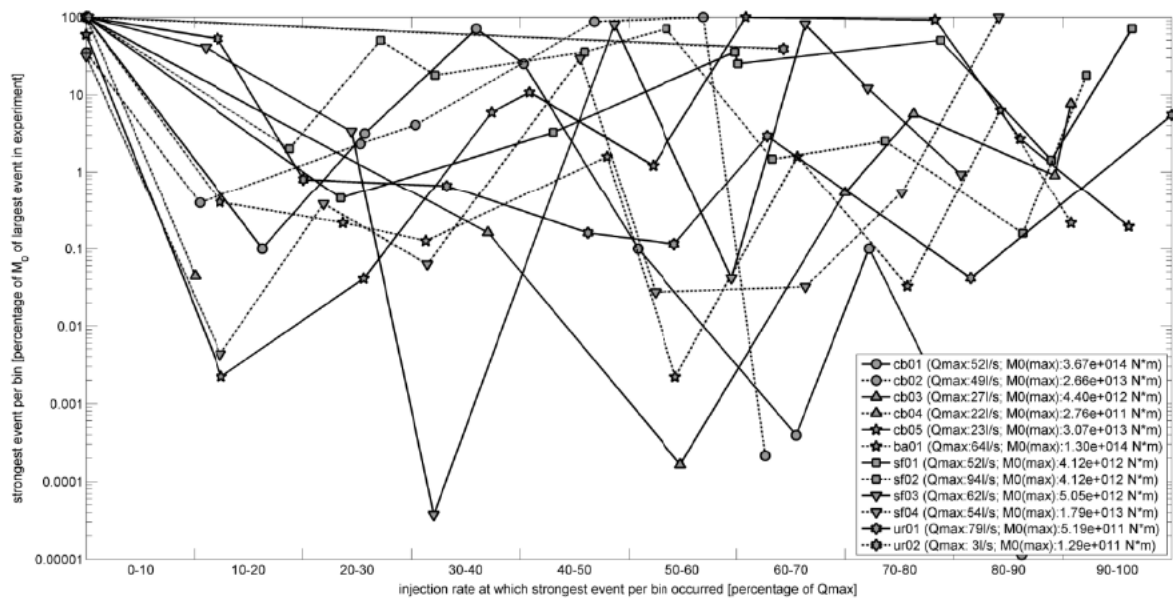


Figure 3: Normalized seismic moment release as a function of the normalized injection rate for the geothermal operations shown in Figure 2. Injection rates are binned at 10 percent intervals of the maximum injection rate operated in each experiment, which is annotated in the legend. For each bin, the earthquake with the largest seismic moment is displayed, with seismic moment stated relative to the maximum seismic moment that occurred in the experiment (listed in the legend). Note that except for cb02, cb05 and sf04, the largest seismic moment release occurred at times of 0 injection rate, i.e. during shut-in. Figure from Baisch et al. (2019).

## 6 CALIFORNIË GEOTHERMAL SITE

### 6.1 Regional Geology

The Californië site is geographically located in the vicinity of the city of Venlo in the south-eastern Netherlands close to the border of Germany. Tectonically it is situated on the Venlo Block, a stable fault block, north-east of the Peel Block and Roer Valley Graben, which are part of the active Roer Valley Rift System (see Figure 4). The Venlo Block is bounded by the Tegelen Fault in the south-west and the Viersen Fault Zone to the north-east (Houtgast & van Balen 2000).

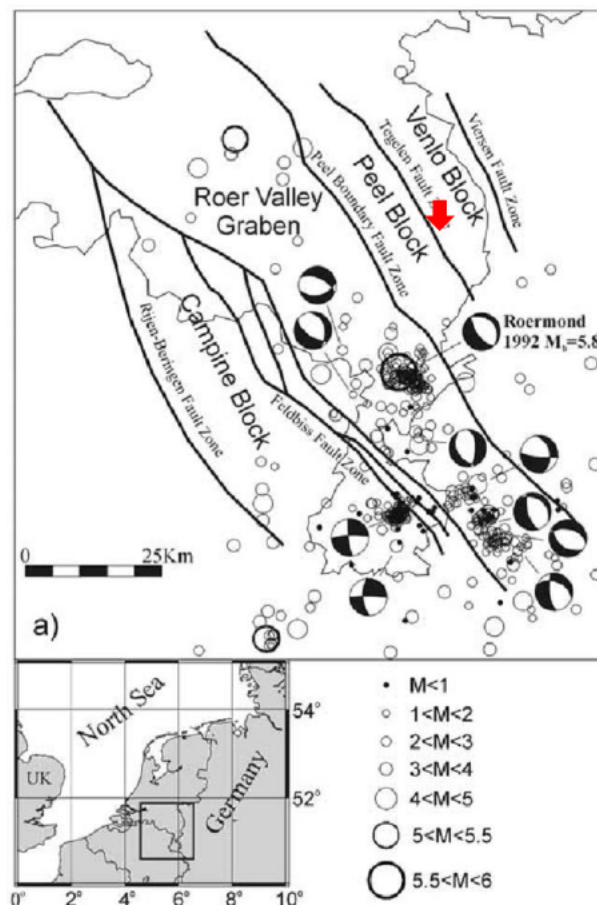


Figure 4: Location of the geothermal project (red arrow) and main structural elements of the Roer Valley Rift System. Earthquakes are denoted by circles. Focal mechanisms after Camelbeeck et al. (1994). The figure is taken from Worum et al. (2004), slightly modified.

### 6.2 Natural Faults

Several faults in the broader vicinity of the project location have been mapped seismically. Fault interpretations were performed by VITO based on two 2D seismic lines (VITO, 2010). Figure 5 shows fault trajectories at the Top Carboniferous Limestone Group and the seismic

lines. The lateral extension of the fault model is limited by the availability of seismic data. For the numerical simulations performed in the current study, fault traces were extrapolated downwards assuming the same (average) dip determined at reservoir level (Figure 6). The Tegelen fault was implemented as a fault zone comprising faults 3 and 5 of Figure 5.

It should be noted that fault trajectories are generally subject to uncertainty given the limited number of seismic lines and their small aperture.

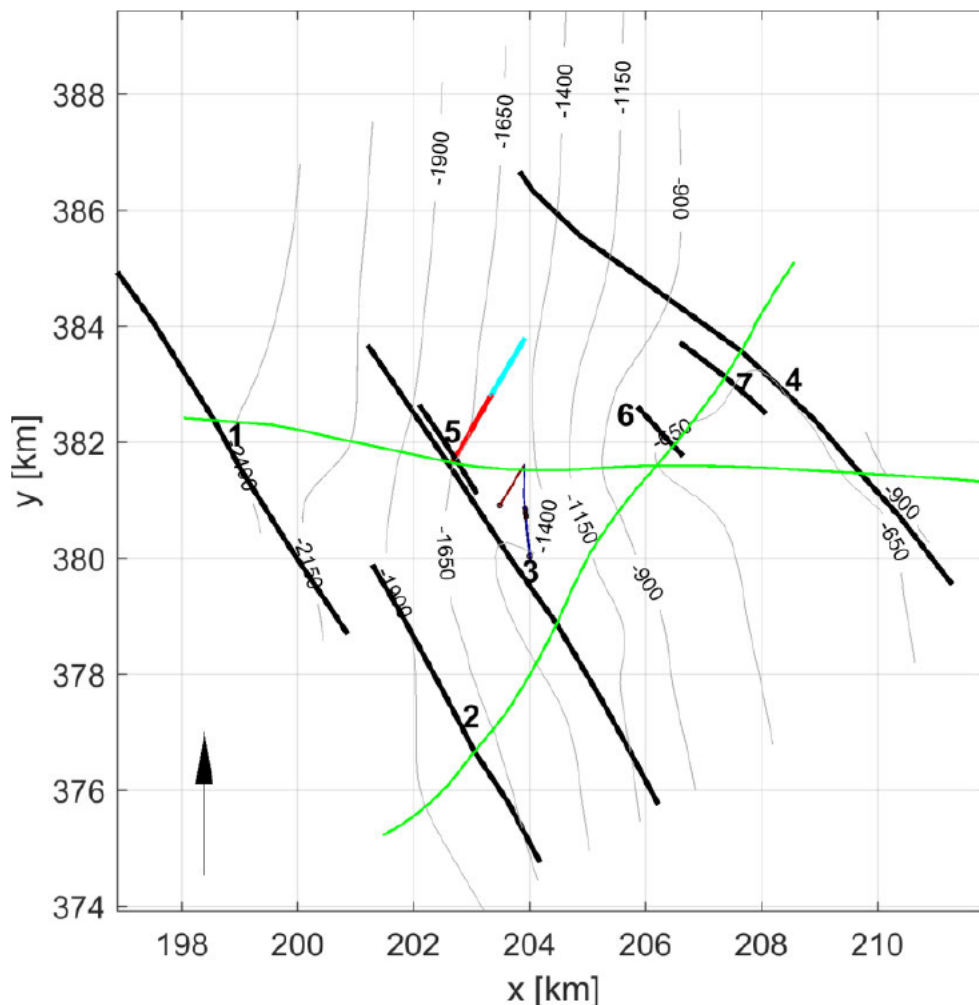
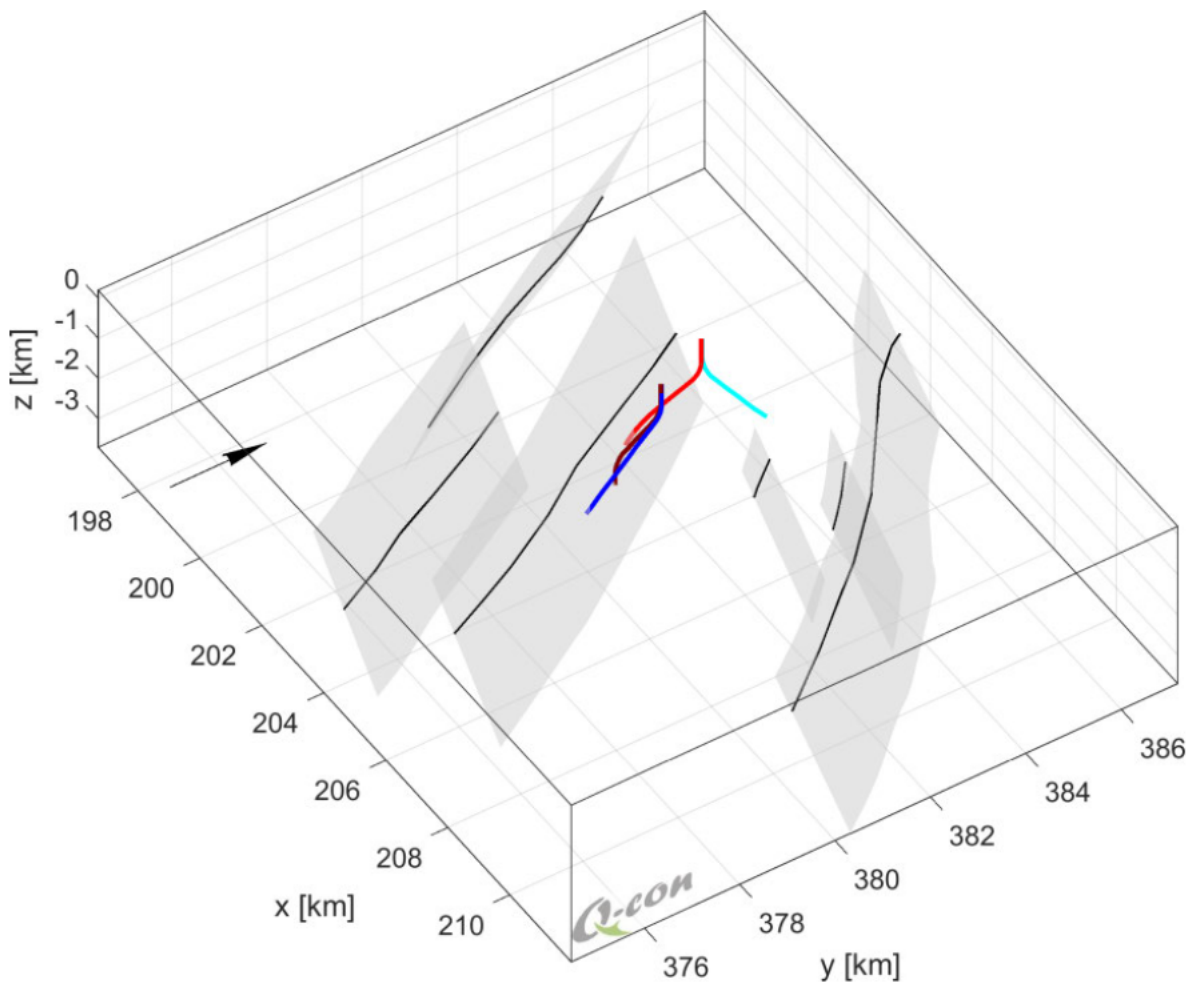


Figure 5: Trajectory of the faults in the vicinity of the reservoir at the Top of the Carboniferous Limestone Group (black lines). The well trajectories of the CWG (red: GT01, blue: GT03) are located close to the Tegelen fault zone (fault no. 3+5) which is the target for producing hot fluid from the subsurface. The well trajectories of the CLG doublet to the North of CWG are depicted in light red (GT04) and light blue (GT05). Seismic lines from seismic surveys depicted in green color. Grey contour lines denote the depth level of the Top Carboniferous Limestone Group. RD coordinates in km.





*Figure 6: Numerical fault model (light grey) derived from the trajectories (black lines) of the faults in the vicinity of the reservoir at the Top of the Carboniferous Limestone Group. The well trajectories of the CWG doublet are plotted in dark red: (GT01) and dark blue: (GT03), the well trajectories of the CLG doublet in light red (GT04) and light blue (GT05). GT01 and GT04 intersect the Tegelen fault zone (center) which is the target for producing hot fluid from the subsurface. The fault trajectories were derived from seismic data. RD-coordinates in km, black arrow denotes Northern direction. RD coordinates in km.*

## 6.3 Stress Field

No measurements of *in situ* stresses were performed at or near the Californië site. On a regional scale, Hinzen et al. (2003) analysed 110 fault plane solutions of natural earthquakes occurring in the northern Rhine area. Their study indicates an average orientation of N125° for the maximum horizontal stress  $S_H$ , consistent with the overall European trend (Plenefisch & Bonjer, 1997; van den Berg, 1994). For the upper 12 km in the Roer Valley Graben, Hinzen et al. (2003) find a vertical orientation of the maximum principal stress. For the depth range between 2 and 5 km, they determine the following stress gradients (Figure 7):

- $\sigma_1$  (here  $S_v$ ): 30 MPa/km
- $\sigma_2$  (here  $S_H$ ): 21 MPa/km
- $\sigma_3$  (here  $S_h$ ): 13 MPa/km

Stress gradients indicate a normal faulting regime for the upper 20 km, which is consistent with fault mechanisms of natural earthquakes determined by Dost & Haak, 2007 (Figure 8).

It has to be kept in mind, however, that the stress field has been determined on a regional (averaged) scale and may deviate on a more local scale. Furthermore, stress gradients may be depth dependent. Stress gradients were determined from natural seismicity typically occurring at greater depth compared to the geothermal reservoir. Therefore, the stress field at reservoir depth may deviate from the model above.

Although not well constrained, the fault plane solution determined for the largest magnitude earthquake near Californië indicates strike-slip failure (Figure 9).

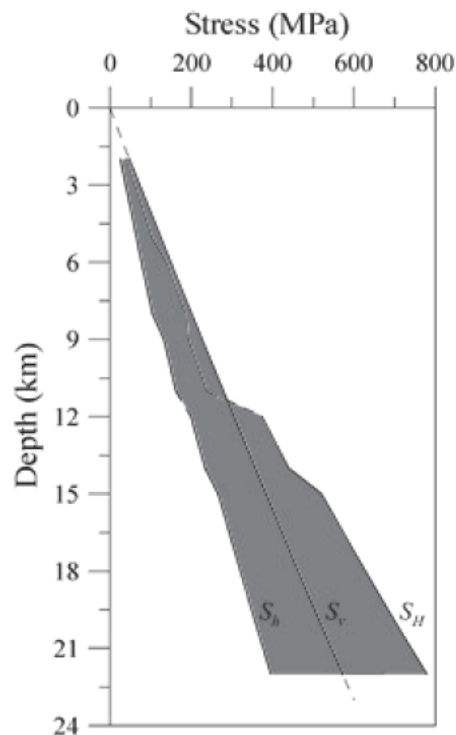


Figure 7: Magnitudes of vertical, maximum horizontal and minimum horizontal stresses,  $S_v$ ,  $S_H$  and  $S_h$  as a function of depth for the lower Rhine embayment. Figure from Hinzen et al. (2003).

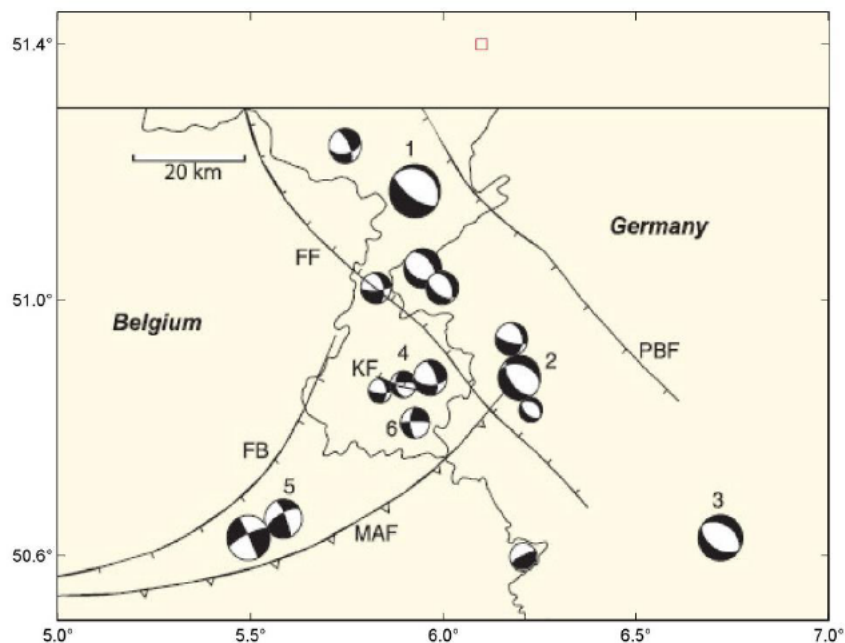


Figure 8: Source mechanisms in and around the Rhine-Valley Graben (from Dost & Haak, 2007, extended towards the North for indicating the project location (red square)). Normal faulting is the dominating mechanism, thus the graben subsides relative to its flanks. (PBF: Peel Boundary Fault, FF: Feldbiss Fault).

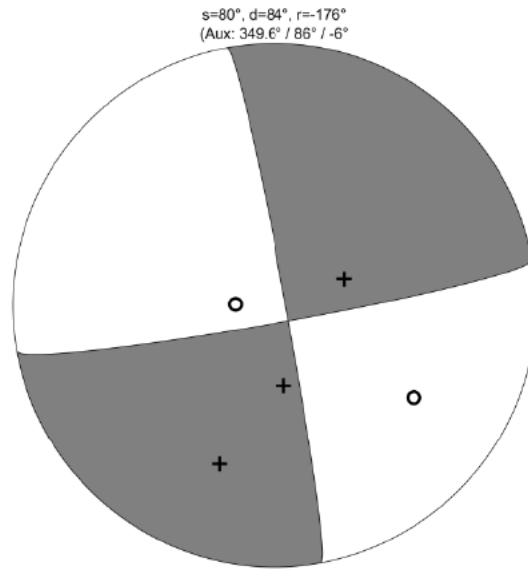


Figure 9: Stereographic projection (lower hemisphere) of the P-phase polarities (plusses indicate compression, circles indicate dilation) of the  $M_L=1.7$  earthquake occurring on 3<sup>rd</sup> September 2018 near the Californië site. The FPS indicates the best matching solution of P-wave polarities and S/P amplitude ratios. The best matching solution indicates a pure strike-slip mechanism on a fault plane oriented approximately consistent with the strike of the Tegelen fault. Figure from Baisch & Vörös (2019).

## 6.4 Stress State on Natural Faults

For a given stress model, the general tendency of faults for failure ('slip tendencies', ST) can be computed. Slip tendencies are defined as (e.g. Yamaji, 2007):

Equation 5: 
$$ST = \frac{\tau}{\sigma_n - p_{fl}},$$

where the notation of chapter 4 is used. Mechanical failure occurs if slip tendencies exceed the coefficient of friction of the fault. Cohesion between failure planes is not considered in this definition.

The magnitudes obtained for ST strongly depend on the model assumptions and are sensitive to absolute stress magnitudes and the orientation of principal stress directions. In general, ST values should only be considered as a qualitative indicator for fault stability since fault strength (i.e. coefficient of friction and cohesion) is generally unknown. The typical range for slip tendencies is between 0.4 and 1.0 (e.g. Zoback et al., 2003).

For the known faults in the vicinity of the project locations, ST values are at the upper end of the typical range when assuming the regional stress field model by Hinzen et al. (2003) introduced in the previous section. When neglecting cohesion all faults are oriented favorably for slip (Figure 10 and Figure 11).

Accounting for the possibility that strike-slip faulting prevails at reservoir level (compare previous section) we note that the general fault orientation (Figure 5) might also be favorable for shear in a NNW-SSE trending stress field.

Since neither stress-strength conditions nor rheological behavior are known, we treat all mapped faults as being (potentially) critically stressed in our hazard analysis. This assumption is supported by the fact that seismicity has already been induced by geothermal operations.

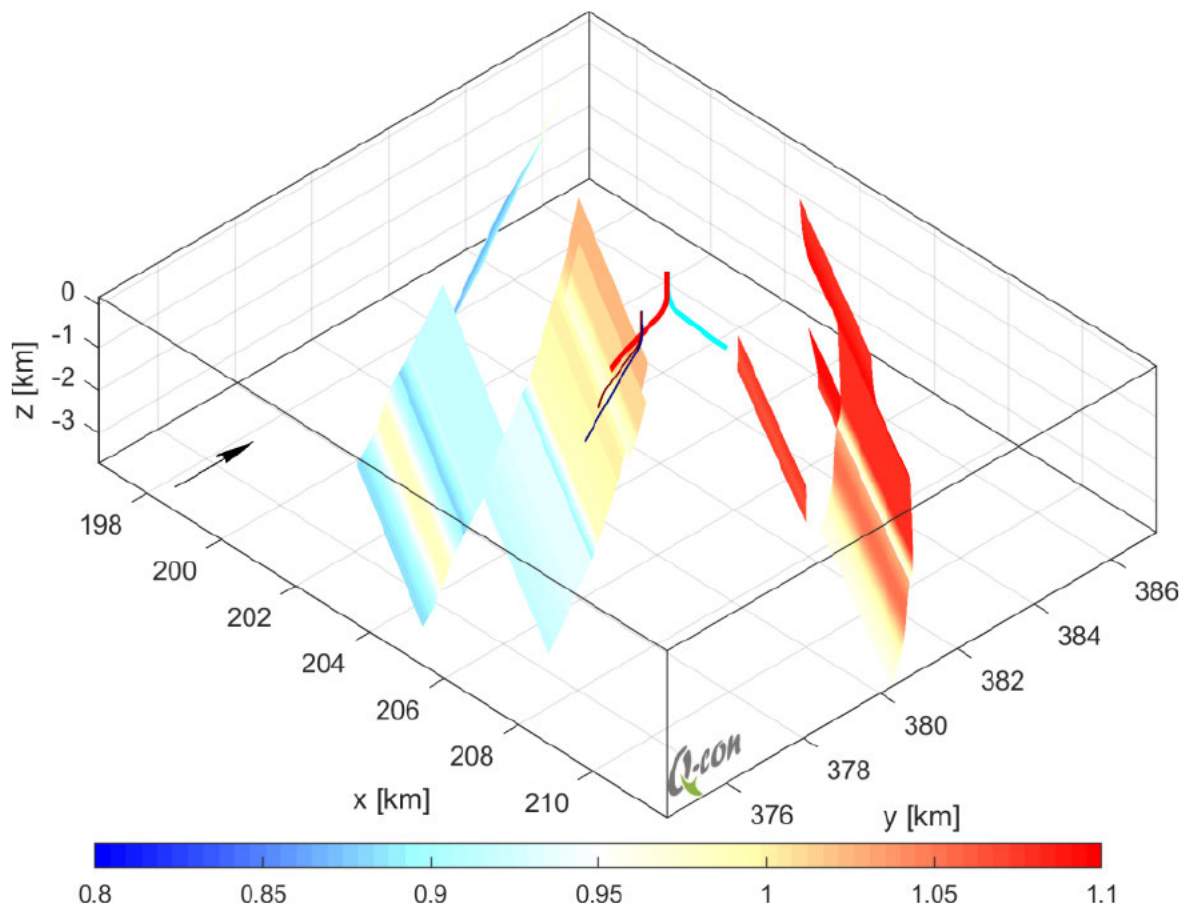


*Figure 10: Slip tendencies (ST) on the faults in the vicinity of the reservoir. The overall level of the ST-values is comparatively high. The highest ST-values are obtained for the Velden fault zone to the NE of the reservoir (up to  $ST=1.1$ ), closer to the CLG doublet. On the Tegelen fault values are close to 1. Production wells GT01 (red) and GT04 (light red) intersect the Tegelen fault, as does the injection well GT03 (blue), which is most likely blocked below the intersection with the Limestone group. Injection well GT05 depicted in light blue. Black arrow denotes northern direction. RD-coordinates in km.*

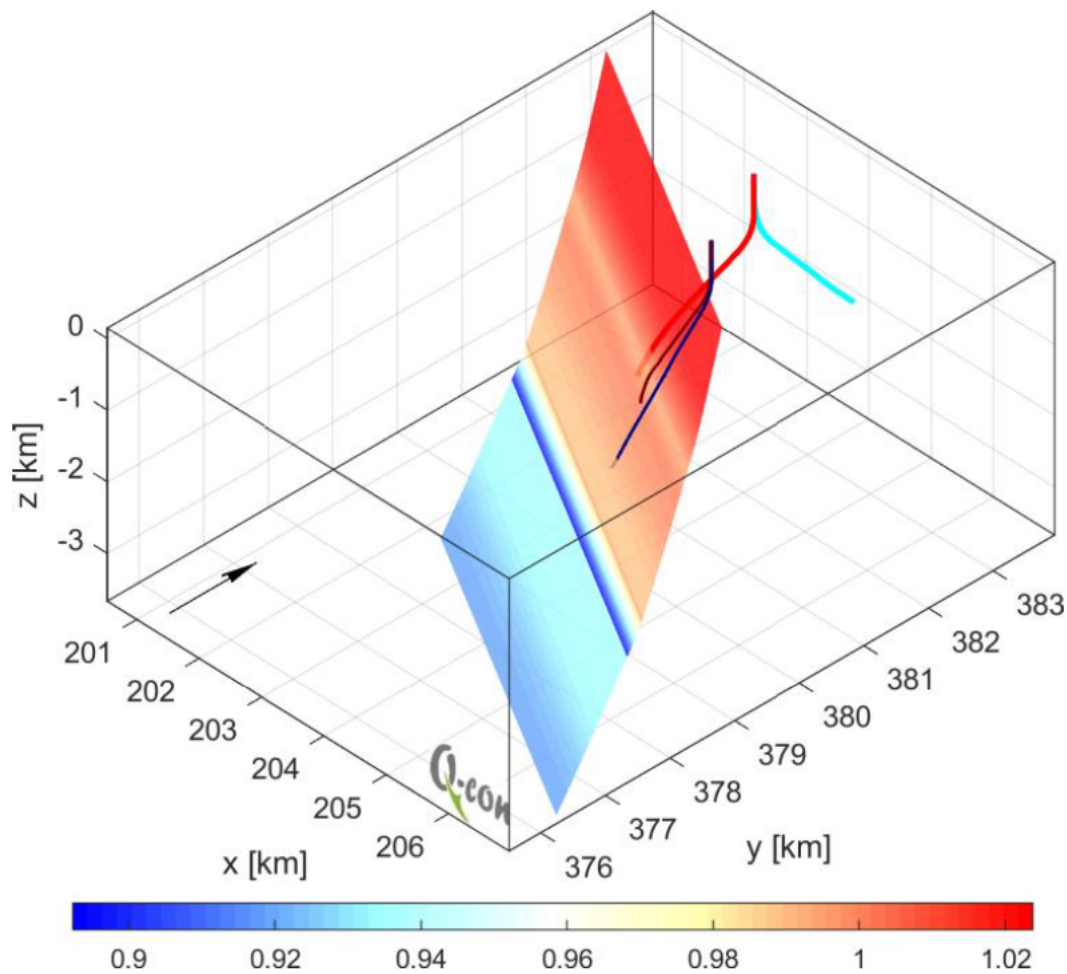


Figure 11: Close up view of slip tendencies (ST) on the Tegelen fault based on the regional stress field. Black arrow denotes northern direction. RD-coordinates in km.

### 6.5 Local Seismicity

Natural earthquakes with magnitude up to  $M_L=4.2$  have been registered at the active Graben structures surrounding the project location (Figure 12). In the closer vicinity of the project location, only few natural earthquakes have been measured. One earthquake ( $M_L=0.8$ ) has been located at a lateral distance of approximately 3 km from the project location with ~15 km hypocentral depth. It should be noted, however, that hypocentral depth is generally not well resolved in this region. In total, 8 natural earthquakes with maximum magnitude of  $M_L=2.2$  within a radius of 20 km have been located around the project location.

Besides natural earthquakes, a total number of 17 local earthquakes in the magnitude range  $M_L=-1.2$  to  $M_L=1.7$  were observed with a local seismic monitoring system (see Rother & Stang, 2015 for description of the system) near Californië (Figure 13 and Table 1). These earthquakes are interpreted to be induced by geothermal activities as discussed in detail by Baisch & Vörös (2019). The primary cause for all but one of the earthquakes was interpreted to be thermal reservoir contraction due to cold water injection at the GT03 well of the CWG-system. At the Tegelen fault near GT03, simulated Coulomb stress changes exceed 1 MPa

at reservoir level (Appendix B.2). At the depth level where the earthquakes have been located (Figure 13), however, the stress impact is much smaller, raising the question if the earthquakes are truly located significantly deeper than the geothermal reservoir. Baisch & Vörös (2019) acknowledge that the uncertainty of the hypocentral depth might be much larger than indicated by the formal inversion error due to unmodelled complexity of seismic wave velocities.

Baisch & Vörös (2019) propose a model, where the timing of induced seismicity is influenced by geothermal production. Pore pressure reduction in the Tegelen fault stabilizes the fault during geothermal production such that stresses resulting from thermal contraction can accumulate on the fault without causing overcritical conditions. When pore pressure recovers during production stop, stress conditions can become overcritical. Only the  $M_L=0$  event #8 (compare Table 1) does not match the proposed mechanism and Baisch & Vörös (2019) conclude that this event could also have been caused by CLG operations.

Time continuous monitoring with the local 5 station network demonstrates that no measurable local earthquakes have occurred since September 9<sup>th</sup>, 2018.



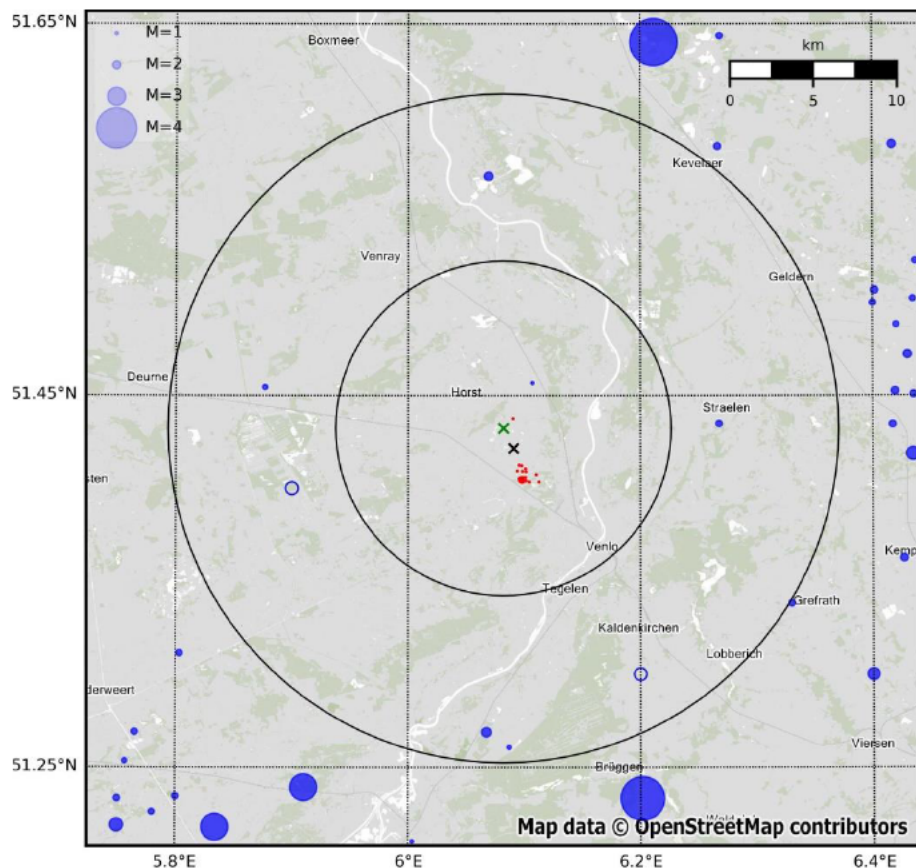


*Figure 12: Location of earthquakes near California (surface locations of CLG and CWG systems depicted by green and black cross, respectively). Induced earthquakes are denoted by magnitude scaled red circles, natural earthquake locations by blue circles. Open circles denote natural earthquakes with no magnitude value assigned. The epicenter of one natural event is located within a 10 km radius (inner circle) of the project location. Eight natural events are located within a 20 km radius (outer circle). Data for natural earthquakes taken from the seismic catalogues provided by BGR (historic) and KNMI as of February 2019 (the induced event from September 2018, listed as natural in the KNMI catalogue, has been removed in this plot). Event epicenters of induced events (including the one removed from the KNMI catalogue) are based on data from the local network.*

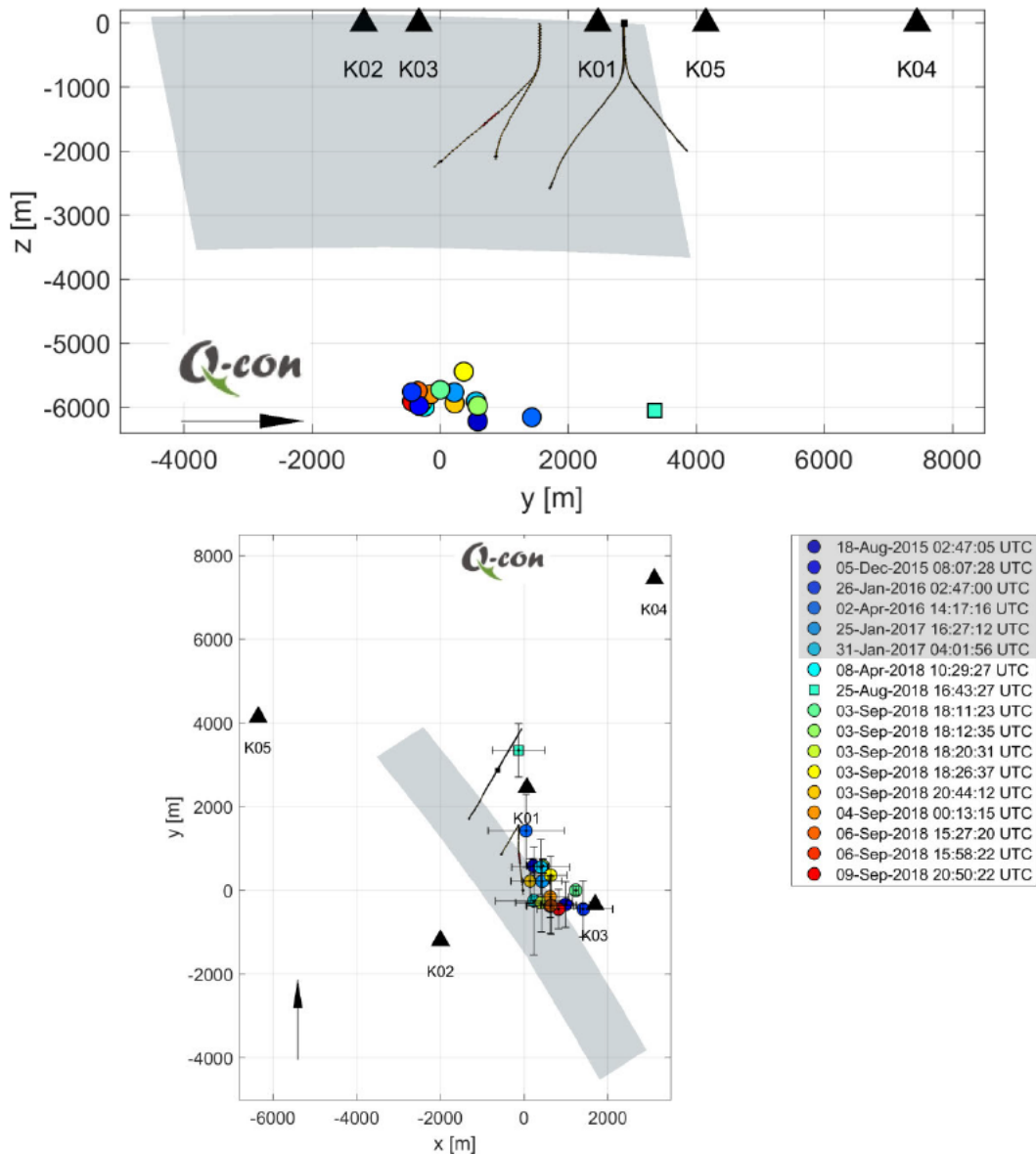


Figure 13: Earthquakes near Californië that are interpreted to be induced by geothermal activities in map view (bottom) and side view (top). Well trajectories and monitoring stations are indicated. Mapped trajectory of the Tegelen fault is displayed by grey shading. Error bars denote  $2\sigma$  confidence limits (formal inversion error). The first 6 earthquakes (denoted by shaded occurrence times in the legend) occurred prior to the production start of the second (CLG) geothermal doublet. Figure from Baisch & Vörös (2019). Reference point of the coordinate system is  $51^{\circ}24'26.85''N / 6^{\circ} 5'31.41''E$ .

#	QUBE event id	date [UTC]	$M_L$	hypocentre location [m] wrt. 51°24'26.85"N / 6° 5'31.41"E 24 m ASL	formal 2 $\sigma$ inversion error [m]
1	596	18-Aug-2015 02:47:05	-0.1	227 586 -6214	178 170 159
2	1	05-Dec-2015 08:07:28	0.3	989 -334 -5974	543 585 716
3	-292	26-Jan-2016 02:47:00	-0.3	1410 -442 -5759	672 711 861
4	400	02-Apr-2016 14:17:16	-0.5	46 1428 -6153	874 905 1353
5	594	25-Jan-2017 16:27:12	-0.3	431 220 -5765	540 468 453
6	593	31-Jan-2017 04:01:56	-0.5	399 559 -5908	656 696 961
7	20274	08-Apr-2018 10:29:27	-0.2	237 -247 -5994	1297 919 1034
8	22363	25-Aug-2018 16:43:27	0.0	-133 3350 -6049	635 628 1090
9	22464	03-Sep-2018 18:11:23	-0.8	1233 0 -5724	108 68 86
10	22442	03-Sep-2018 18:12:35	-0.4	446 585 -5974	167 122 126
11	22438	03-Sep-2018 18:20:31	1.7	414 -291 -5924	706 614 663
12	22443	03-Sep-2018 18:26:37	-0.3	632 368 -5442	444 386 425
13	22465	03-Sep-2018 20:44:12	-1.0	143 224 -5931	525 453 429
14	22466	04-Sep-2018 00:13:15	-1.2	622 -152 -5793	495 444 411
15	22498	06-Sep-2018 15:27:20	-0.4	643 -354 -5744	689 599 643
16	22499	06-Sep-2018 15:58:22	-0.5	621 -374 -5810	650 564 603
17	22484	09-Sep-2018 20:50:22	0.0	826 -443 -5904	467 513 624

Table 1: Local earthquake catalogue. Coordinates refer to absolute hypocentre locations. Coloured shading of event numbers indicates periods where only CWG (light blue), both, CWG and CLG (dark blue) or CLG only (violet) were in operation. Grey shading denotes that both doublets were not operating. Table from Baisch & Vörös (2019).

## 6.6 Geothermal Operations

Testing of the CLG wells GT04 and GT05 started in summer 2017 (Figure 14). A long-term circulation test between GT04 (producer) and GT05 (injector) commenced in September 2017 and was stopped in August 2018. During the testing period, the CWG doublet system has been in continuous operation until May 2018 (Figure 14 and Figure 15).

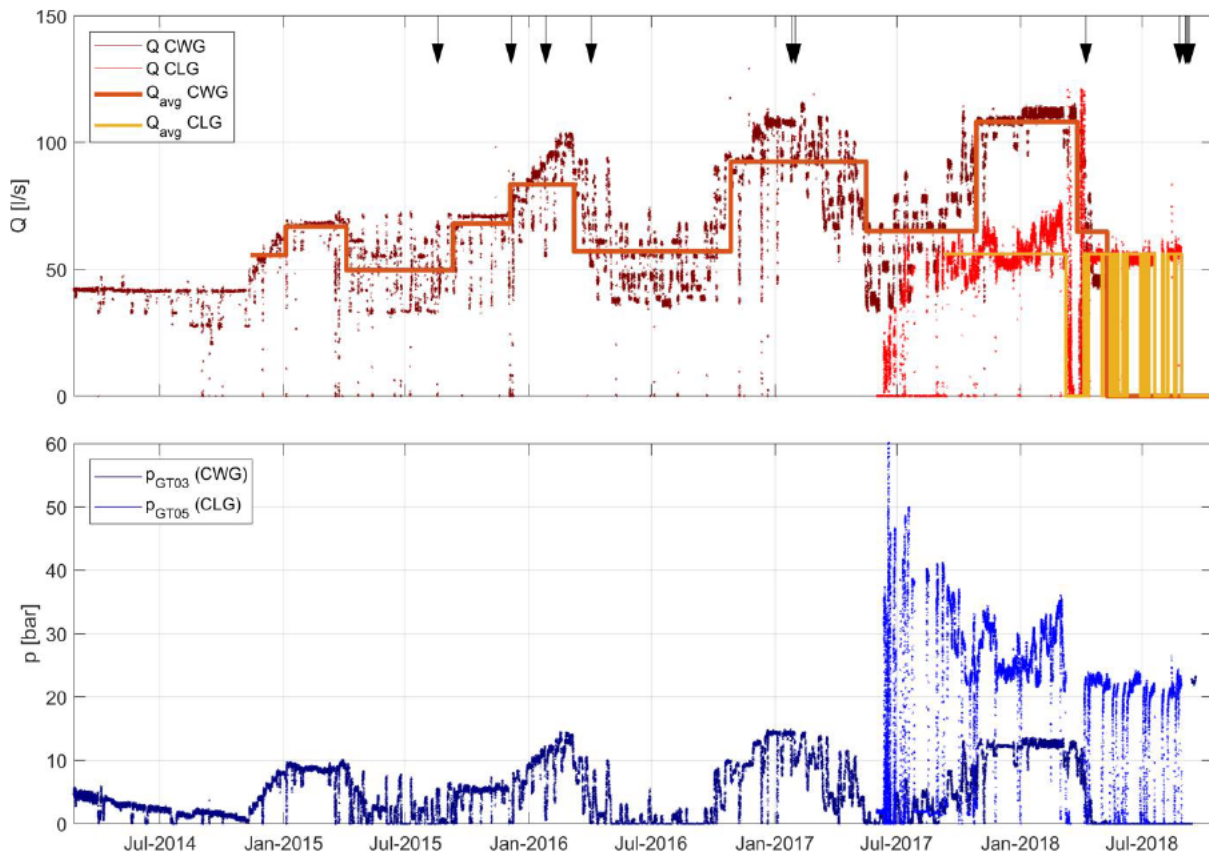


Figure 14: Flow rate (top) and wellhead pressure (bottom) at the injection wells GT03 (CWG) and GT05 (CLG). The data cover the time window between the start of operations of the CWG doublet in February 2014 and stop of operations at the CLG doublet in August 2018. Averaged flow rates used for numerical simulations are indicated by solid lines according to the legend. The occurrence times of induced earthquakes are denoted by black arrows.

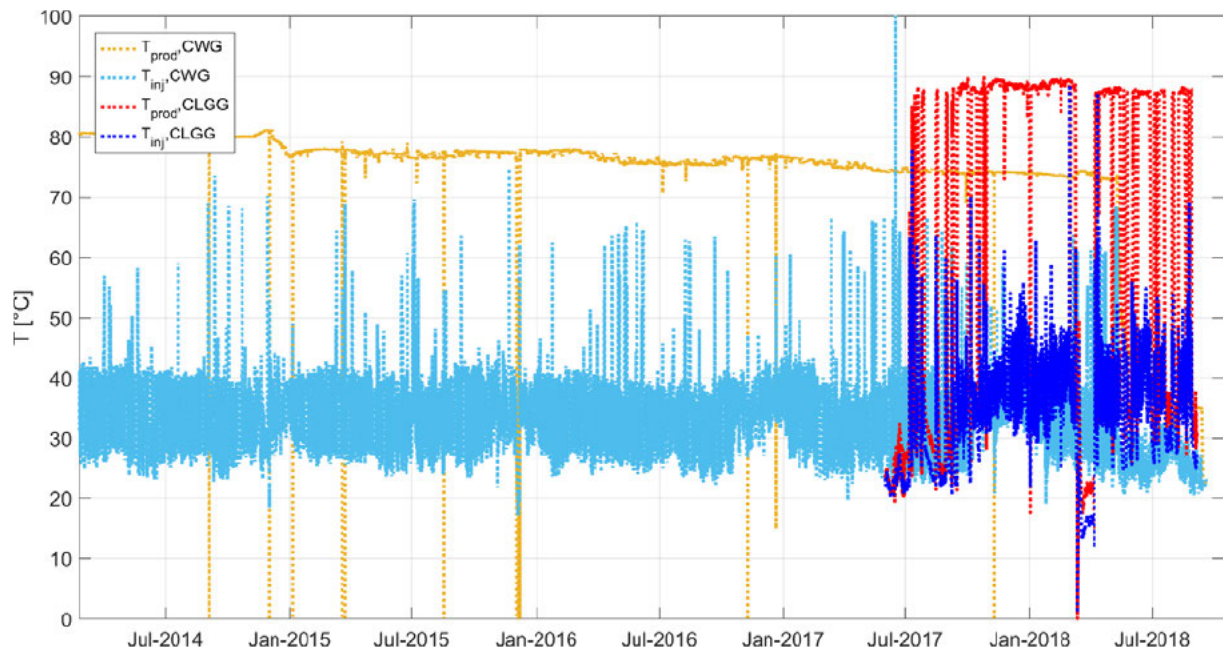


Figure 15: Injection- and production temperature at the CLG and the CWG doublet, respectively.

## 7 CALIFORNIË RESERVOIR MODEL

### 7.1 VITO Model

Based on hydraulic data gathered during the tests, VITO has developed a reservoir model, which was provided to Q-con in digital form (VITO, 2018). The model consists of 8 layers and the trajectories of the Tegelen and Velden fault (Figure 16).

Fault number 6 and 7 in Figure 5 are interpreted as being artifacts in the seismic interpretation by VITO and are not included in the VITO reservoir model. Figure 17 to Figure 18 show the elements of the reservoir model. The reservoir layers are dipping West-South-West and tend to thin-out towards the North and the East.

Table 2 gives an overview of which well connects to which formation through its openhole section. The two doublet systems utilize different reservoir layers. The southern CWG doublet GT01/GT03 targets the L2/L3/L4 layers of the Zeeland group and fluid is primarily produced from the highly permeable Tegelen fault (VITO, 2018), although the open hole section of the production well extends over layers L2 and L4. The northern CLG doublet GT04/GT05 targets layer L5 of the Zeeland group and the formations Pont d'Arcole (PdA), Bosscheveld (BO) and upper Condroz (COres). Fluid is also primarily produced from the highly permeable Tegelen fault (VITO, 2018).

Although both doublets are operated in different reservoir layers, hydraulic interferences are possible since the reservoir layers are hydraulically connected in the southern part of the model and through the Tegelen fault.

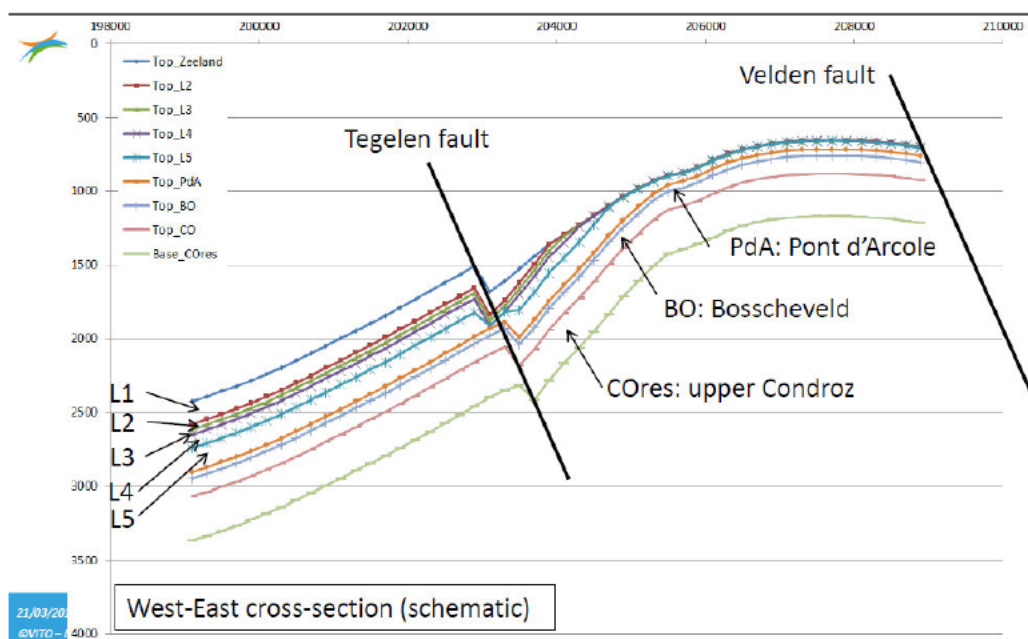


Figure 16: Schematic West-East cross-section through the VITO reservoir model. Source: VITO (2018).

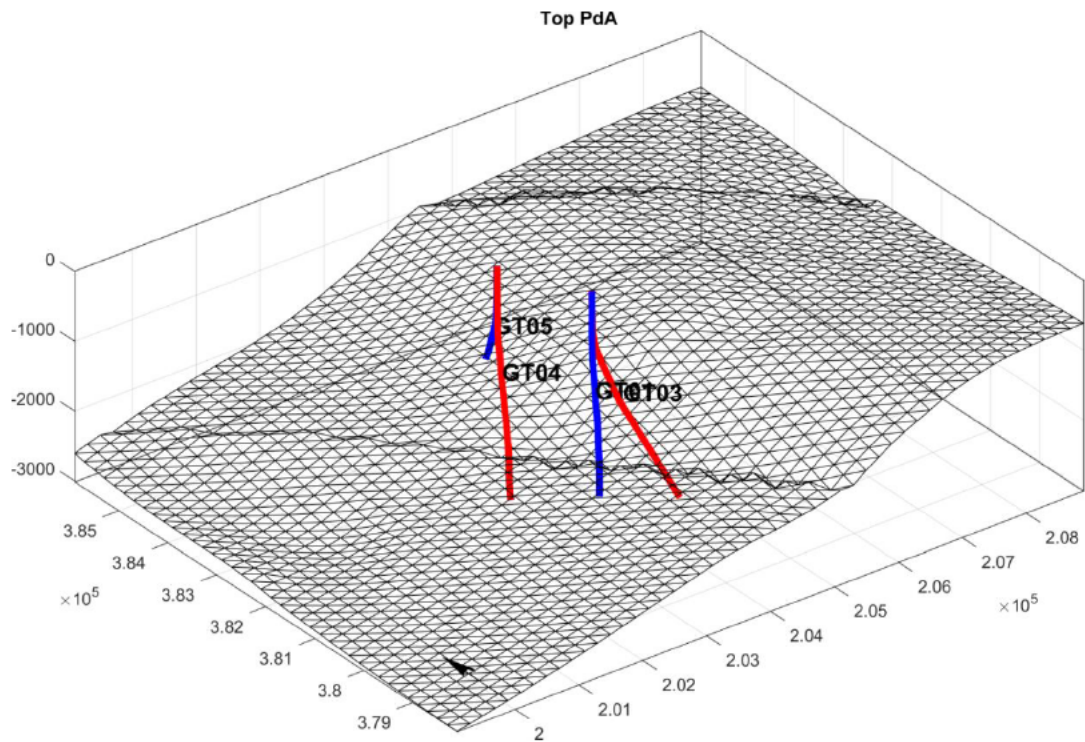


Figure 17: Triangulated Layer (Top PdA) and well trajectories. The two layer offsets indicate the location of the Tegelen fault to the West and the Velden fault to the East.

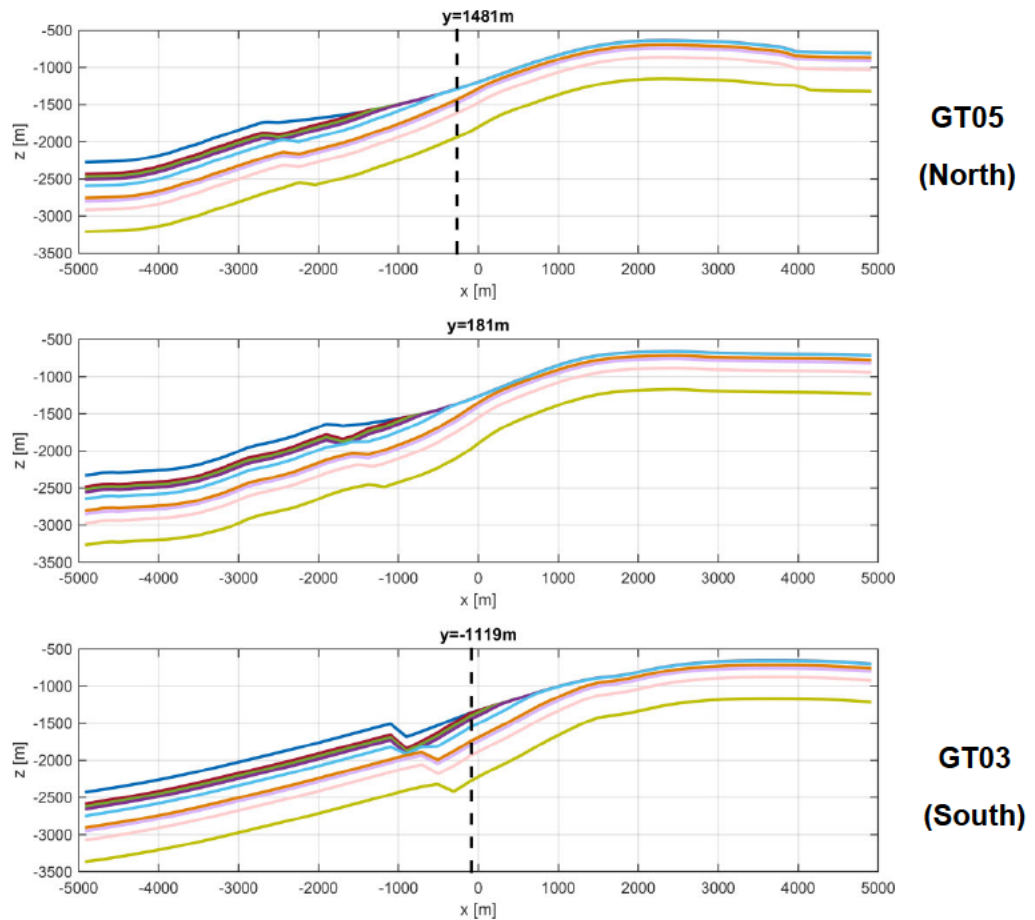


Figure 18: EW-depth section through the reservoir. Upper and lower section are at the well locations GT05 and GT03, respectively (dashed black lines). Note the thinning-out of the L1-L5 reservoir layers towards the North. Coordinates in meters in a local coordinate system.

Layer		open hole	
		CLG	WSC
Zeeland	L1		
	L2		GT03
	L3		
	L4		GT03 / GT01
	L5	GT05	GT01
PdA		GT05	GT01
BO		GT05	GT01
COres		GT05 / GT04	GT01

Table 2: Structural reservoir model and open-hole sections of the wells. Producers and injectors are marked in red and blue, respectively.



## 7.2 Model Implementation

For the current hazard analysis, the VITO reservoir model (section 7.1) was geometrically simplified. This reduced computational effort, allowing sensitivity testing of the model elements in an acceptable timeframe. The sensitivity tests ensure that conclusions derived from modeling results are not critically depending on geometrical details of the model, which might not be (entirely) calibrated by observation data.

The geometrically simplified model preserves the main characteristics of the VITO model such as average layer thickness, hydraulic properties and distances between wellbores and faults. Simulated hydraulic pressure during geothermal production is mainly depending on these primary characteristics and is not sensitive to details of the layer topography. Computational efficiency was increased by projecting the dipping layer stack into the horizontal and by implementing vertical fault trajectories.

For the current hazard analysis it is of particular interest to what extend geothermal operations change the fluid pressure on the Tegelen and the Velden faults. The hydraulic properties of the Velden fault, however, are unknown. Possible end-member scenarios are a sealing and a highly conductive Velden fault. Both scenarios are considered and discussed in the current study, whereas in the base model, the Velden fault is assigned the same hydraulic properties as the surrounding rock.

The simplified reservoir model was implemented into the FE simulation software COMSOL Multiphysics (Figure 19). Due to the limited lateral extension of the VITO model, the Velden fault is located near a model boundary and simulation results are depending on the assumed boundary condition. As part of our sensitivity analysis, we consider the two end-member scenarios of a constant pressure and a no-flow boundary.

Table 3 lists the permeability and porosity values of model. For all simulations, constant fluid parameters were assumed (viscosity  $4.4 \cdot 10^{-4}$  Pa·s, compressibility  $4.3 \cdot 10^{-10}$  1/Pa). These correspond to the average depth level of the reservoir at the GT05 location, a temperature gradient of 33 °C/km and 11°C surface temperature. Simulations of previous geothermal operations are based on the smoothed flow rate shown in Figure 14. Parameters used for the simulation of future geothermal operations are provided in Table 4 and Table 5 lists the parameters used for the simulation of thermal reservoir contraction.

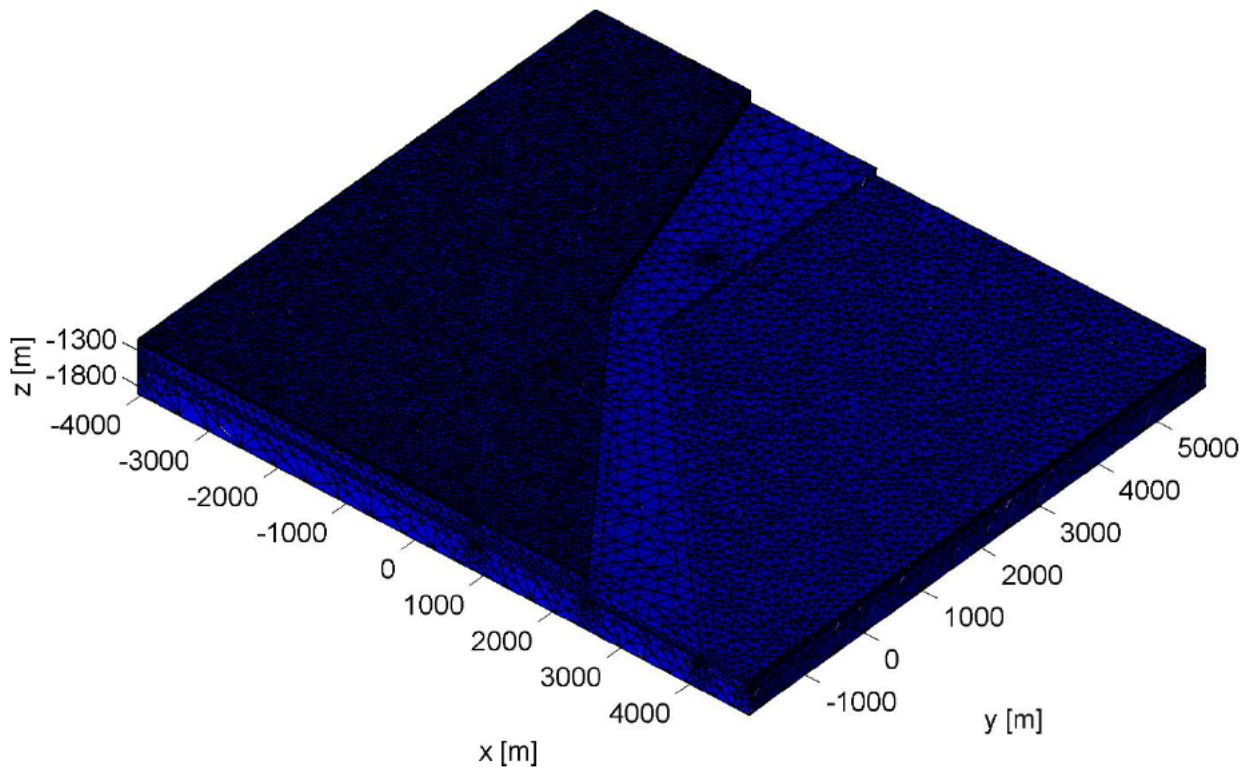
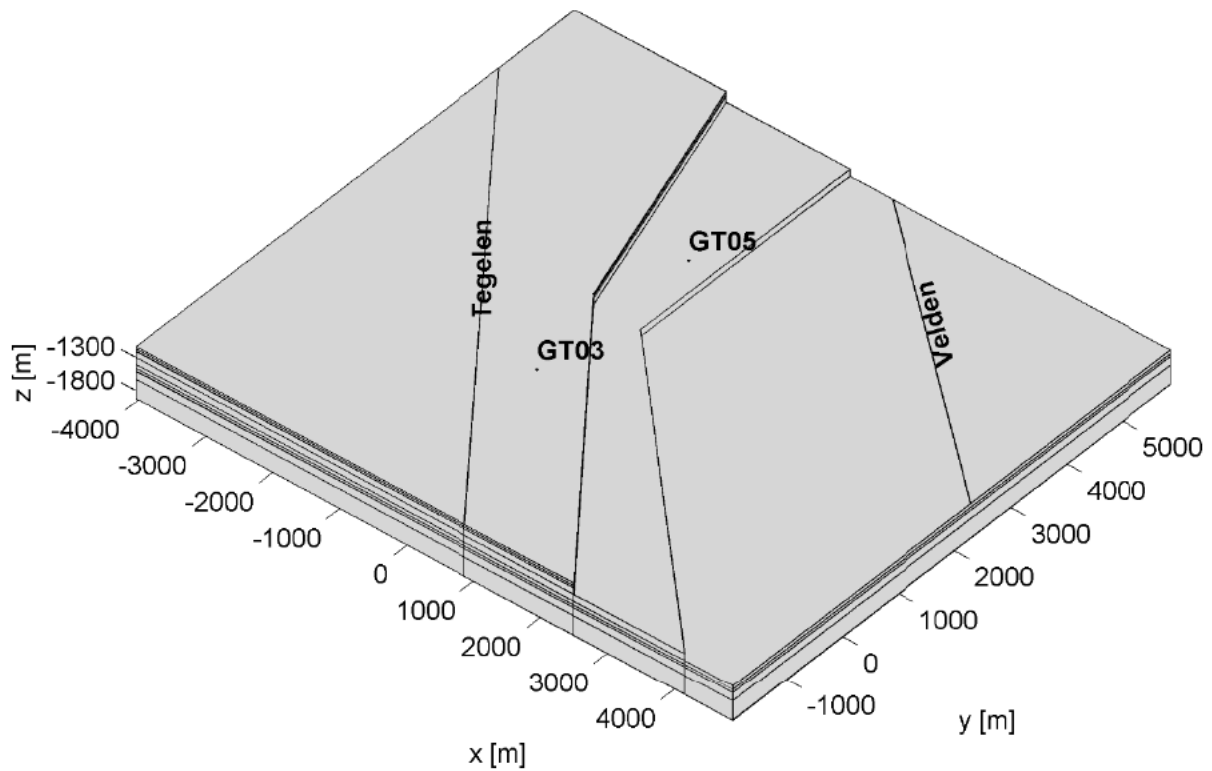


Figure 19: Numerical model geometry (top) and finite element mesh (bottom). The two regions with a dense mesh indicate the locations of the injection wells GT05 and GT03. The production wells are implemented as point sources which do not require a denser mesh.

Layer / Fault	Permeability [m <sup>2</sup> ]	Porosity [%]	Average Thickness [m]
L2	6.2e-13	4	35 / 0
L3	9.8e-16	1	35 / 0
L4	1.2e-13	1	90 / 0
L5	4.2e-15	1	160 / 56
PdA	9.9e-16	1	44
BO	5.7e-15	1	122
COres	1.9e-14	1	290
Tegelen fault	4.5e-13	4	200

*Table 3: Hydraulic model parameters after VITO (2018). Note, layer L1 was not implemented due to its negligible permeability. Layers L2 to L5 'edge out' towards the center of the model. Average thickness in the western and the eastern part of the model are stated in the table.*

parameter	value
average flow rate	200 m <sup>3</sup> /hrs
production temperature fluid	88°C
re-injection temperature fluid	40°C

*Table 4: Hydraulic parameters used for the simulation of future geothermal operation of the CLG doublet.*

parameter	value
density reservoir rock	2500 kg/m <sup>3</sup>
specific heat capacity	900 J/kg/K
linear thermal extension coefficient	8.0 · 10 <sup>-6</sup>
shear modulus	20 GPa
Poisson's ratio	0.25
coefficient of friction	0.6

*Table 5: Rock parameters used for the simulation of thermal contraction and associated stresses.*

## 8 SEISMIC HAZARD

Basic physical considerations reveal that the seismic hazard is driven by stress perturbations related to the geothermal system in combination with the existence of seismogenic faults in the subsurface (section 4). In the current context, the most relevant sources of stress perturbations are elevated pore pressure and stresses induced by thermal reservoir contraction. Other sources of stress changes as listed in section 4 are either not applicable (mass changes) or considered to have only a secondary impact due to their short-ranging nature (chemical processes). Given the small amplitude of hydraulic pressure perturbations with respect to total stresses, poro-elastic effects are also considered to be of secondary order.

In a first step we use numerical simulations of hydraulic pressure and thermal reservoir contraction to investigate Coulomb stress changes on the known (Tegelen and Velden) fault (sections 8.1 and 8.2). Simulations of previous geothermal activities provide an estimate of the critical level of Coulomb stress changes at which earthquake activity has occurred. This critical level is compared to the simulated Coulomb stress changes associated with 20 years of continuous production of the CLG doublet (assuming no further operations of the CWG doublet). The associated seismic hazard is discussed in section 8.3, where we also consider the possibility of additional, undetected faults and discuss uncertainties. A traffic light system for risk mitigation is proposed in section 8.3.4.

### 8.1 Hydraulic Overpressure

Elevated pore pressure resulting from re-injecting fluid during geothermal production can cause seismicity (chapters 4 and 5). In the simple scenario where only the pore pressure in a fault changes by geothermal activities while shear- and normal stresses and fault strength remain constant, the occurrence of seismicity is restricted to those locations where virgin pressure conditions are exceeded (Equation 1).

Regions of elevated pore pressure (above virgin conditions) predominantly exist in the vicinity of an injection well. The CLG doublet produces from the Tegelen fault and re-injects fluid at a location with no mapped faults within 2 km distance (Figure 5).

We use the numerical model described in section 7.2 to simulate the hydraulic pressure evolution during previous geothermal production as well as for a future 20 years production scenario. *Figure 20* shows the temporal evolution of simulated hydraulic pressure at different fault locations. The simulation is based on an end-member model with no-flow boundaries which maximizes the pressure amplitude on the faults. In this model, overpressure on the Velden fault has reached a maximum level of approximately 5 bar within the first 3 month of CLG production. A similar pressure evolution is also observed at the potential location of faults #6 and #7, although we note that these faults are not part of the VITO reservoir model.

In a future production scenario, this pressure level is not exceeded (*Figure 25*). Following the concept of the Kaiser effect (chapter 5), no seismicity occurs at those locations where quasi-stationary hydraulic conditions have been reached, provided that no other source of stress-change is acting at this location. Our simulation results demonstrate that quasi-stationary

hydraulic conditions have been reached in the entire model during previous geothermal activities. This conclusion is independent of a particular choice of boundary conditions (compare *Appendix B.1*).

Hydraulic pressure on the Tegelen fault is generally reduced during geothermal production (*Figure 20*) and returns to its virgin state after production stop.

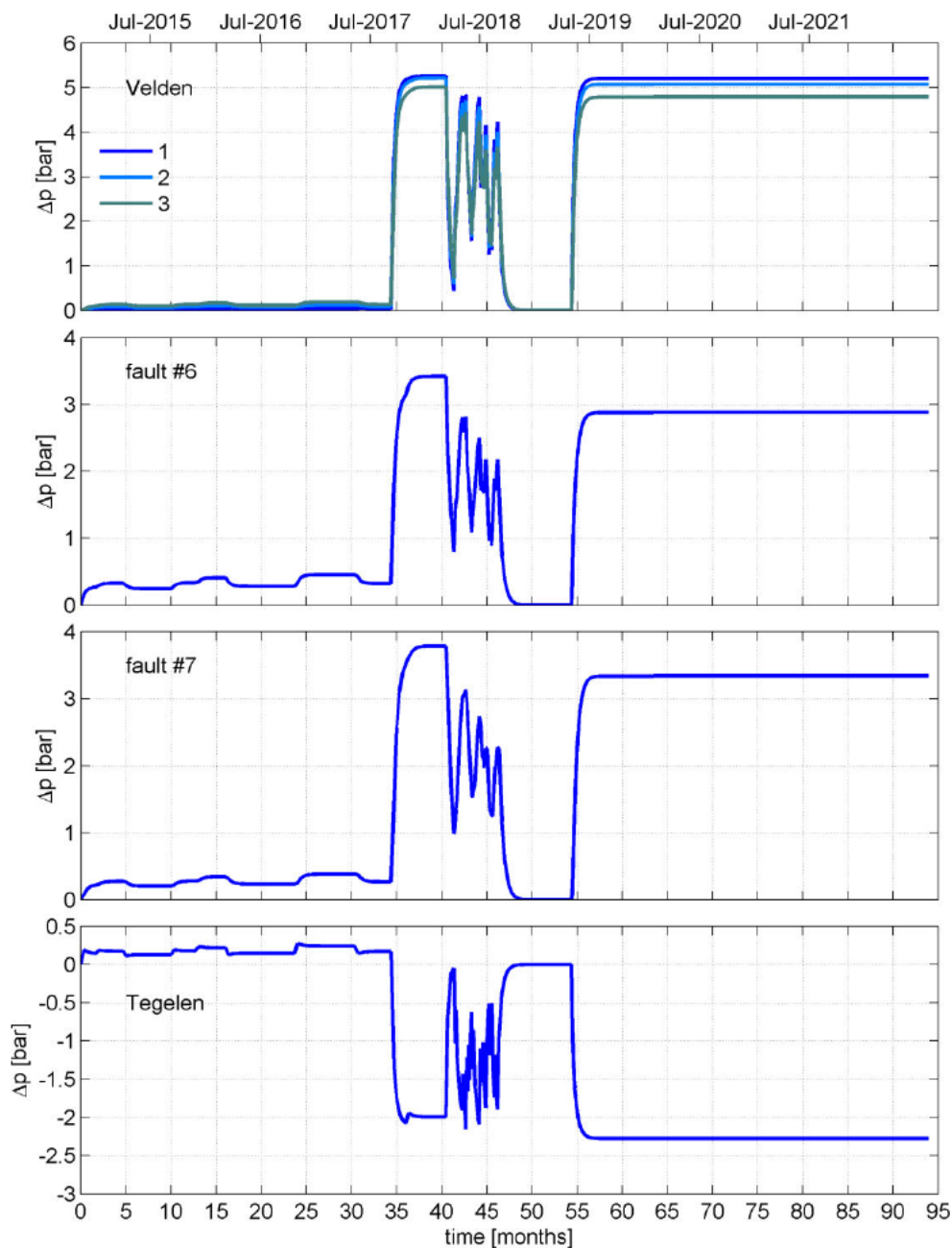


Figure 20: Numerically simulated hydraulic pressure evolution during previous geothermal production and for a future CLG production scenario. Pressure is shown at different locations on the mapped faults as indicated in Figure 24. No-flow model boundaries were assumed, maximizing the amplitude of overpressure (results for alternative modeling assumptions are provided in Appendix B.1). Average CLG flow rates were used as indicated in Figure 14. The initial CLG testing phase with strong variations of production rate was deliberately ignored. Ignoring the initial testing phase implies that actual quasi-stationary conditions tend to be reached later with the current simulations (conservative perspective). Future production has been simulated for 20 years but is shown for 3 years only as the pressure level reached its maximum already after a few months' time.

## 8.2 Thermal Reservoir Contraction

The stress impact resulting from thermal reservoir contraction has been simulated for the previous geothermal production phase as well as for a future 20 years production scenario using the parameters specified in section 7.2.

Simulations are based on semi-analytical solutions sources (Okada, 1992) where a contraction source is initially centered at the GT05 injection point. The contraction source exhibits the same (average) dip as the upper Condroz layer, which is the most conductive layer (section 7.1). The source volume is growing spatially with time, approximating the propagation of the cooling front. Within the source volume, isotropic contraction is assumed which is simulated by super-imposing three orthogonal Okada-type sources.

To limit the number of Okada type sources required to approximate complex geometries, the vertical extension of the cooling front into neighboring layers is neglected while preserving total contraction. This approximation is conservative with respect to seismic hazard as the Coulomb stress changes on the known faults tend to be larger due to a larger lateral extension of the cooling front (implying a shorter distance to the faults).

Coulomb stress changes  $\Delta CS$  have been simulated on the faults closest to the injection well GT05. These are the Tegelen fault to the West and the Velden fault as well as fault #6 and #7 to the East (Figure 5). As stress magnitudes predominantly depend on the distance to the contraction source, resulting stress perturbations on the remaining, more distant faults are smaller. Accounting for uncertainties regarding the stress field (section 6.3), all simulations were performed for a normal-faulting, as well as for a strike slip regime. Associated figures are provided in Appendix B.2.

During the previous testing phase, simulated Coulomb stresses are extremely small on the known faults and are in the order of  $10^{-2}$  bar or less in all models (Figure 26 to Figure 33).

In a future production scenario, the level of  $\Delta CS$  on the known faults generally remains smaller than 0.26 bar (maximum value on the Tegelen fault, Figure 21). At the section of the Tegelen fault where the previous seismicity cluster was located,  $\Delta CS$  is a few hundred Pa only. For comparison, simulated stress changes on the Tegelen fault resulting from the previous operation of the CWG doublet are orders of magnitude larger (Figure 34).



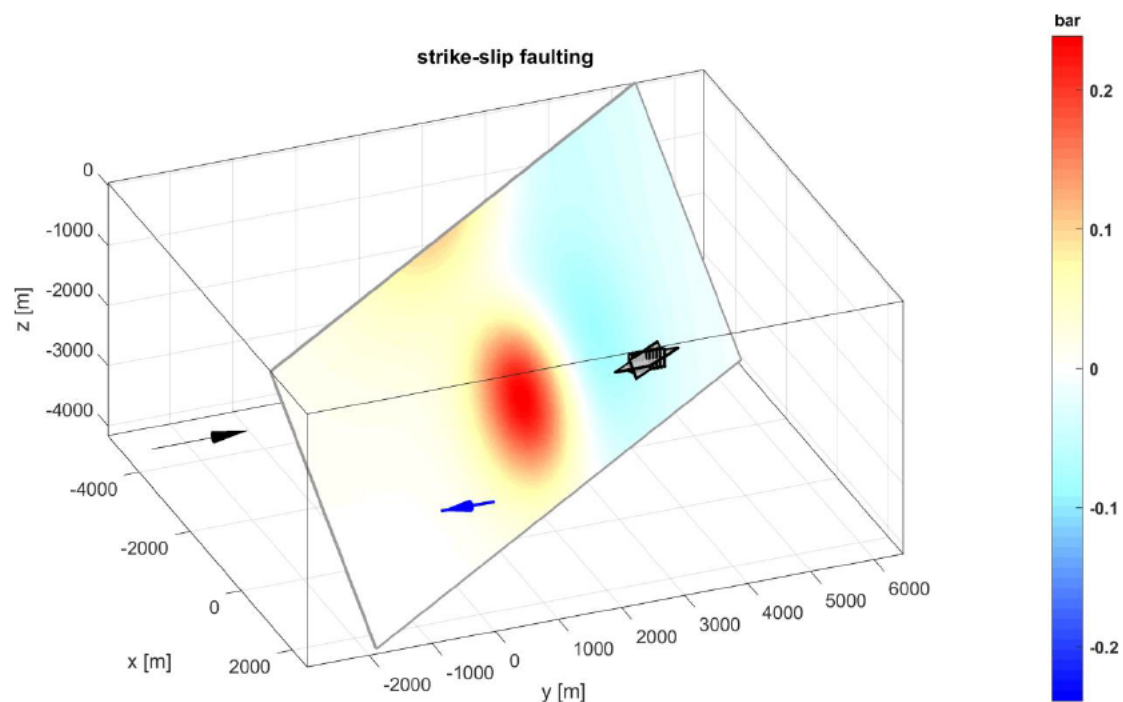


Figure 21: Simulated Coulomb stress changes according to color scale on the Tegelen fault after a future production of the CLG doublet over 20 years. Strike slip failure is assumed. Okada source displayed by grey rectangles, blue arrow denotes approximate lateral location of previous seismicity.

## 8.3 Hazard Assessment

### 8.3.1 Seismicity Potential

At the Californië location, mapped subsurface faults are generally oriented favorable for shearing (section 6.4) and we consider it likely that larger sections of these faults are critically stressed. This assumption is supported by the occurrence of induced seismicity.

In a previous study, Baisch & Vörös (2019) interpret observed seismicity at Californië as being due to thermal contraction caused by cold water injection near the Tegelen fault through CWG well GT03. The level of (contraction) stresses at which seismicity was induced, however, is not finally clear due to the uncertainty of the depth location of the earthquakes. At reservoir level, the stress changes are in the order of  $\Delta CS=10$  bar (Figure 34), which is considered to be a plausible level at which seismicity can be induced (chapter 4). If the earthquakes occurred at greater depth, however, the level of stress changes is significantly lower. Although it cannot be completely ruled out, we consider it unlikely that these earthquakes were caused by stress changes smaller than 1 bar.

Numerical simulations of hydraulic pressure indicate that the maximum fluid pressure on the faults during future CLG production does not noticeably exceed the pressure level obtained during previous production. Following the concept of the Kaiser effect (chapter 5), no seismicity caused by overpressure is expected for the future production scenario, provided that no other source of stress change is acting, such as thermal contraction. On the known faults,

simulated stress changes resulting from thermal contraction are in the order of 0.2 bar and are considered to be too small to cause seismicity.

Within the framework of our subsurface model ('expected case'), we therefore conclude that no induced seismicity is to be expected in the future production scenario.

We do, however, acknowledge the uncertainty associated with our subsurface model. Most noticeably, seismicity could be induced on an undetected fault near the CLG injection well. Numerical simulation results demonstrate that hydraulic pressure conditions on any hypothetical fault close to the injector reached quasi-stationary conditions already during the testing phase (section 8.1). As fluid pressure does not exceed previous pressure values in the future production scenario, no seismicity caused by overpressure is expected on a hypothetical fault near the injector. This conclusion is independent on the geometry of the hypothetical fault and its hydraulic properties. It also applies to the hypothetical case of a 'pressure channel' establishing an efficient hydraulic connection between the injector and the Tegelen fault.

Cold water injection close to such a hypothetical fault, however, could result in significant Coulomb stress changes on the fault due to thermal contraction. In this case, seismicity could occur and the magnitude of induced earthquakes is expected to increase with time following the gradual growth of the fault area subjected to positive Coulomb stress changes.

This scenario is similar to the one discussed for the CWG cold water injection. A fundamental difference, however, is that the CWG doublet produced from the seismogenic fault. This can lead to a certain type of trailing effect, where Coulomb stress changes accumulate on the fault while a seismicity response occurs only post-production when fluid pressure increases (compare section 6.5). For a hypothetical fault close to the CLG injector, this type of trailing effect is not relevant implying a better efficiency of the traffic-light system proposed for risk mitigation (section 8.3.4).

Finally we note that future seismicity might occur at Californië even without any further geothermal operations. Stress-strength conditions in the vicinity of previous seismicity are most likely near-critical. Small-scale stress diffusion similar to the process of 'after deformation' as well as external stress perturbations could lead to future seismicity. The absence of measurable seismicity over the last 6 months, however, may indicate that stress conditions have already returned to a stable state.

### 8.3.2 Metric

Following the recommendations for seismic hazard assessment of geothermal systems in The Netherlands (Baisch et al., 2016), we have chosen peak ground vibration (PGV) as a metric for assessing hazard. According to Dutch engineering standards (SBR, 2010), damage to ordinary buildings is considered to be unlikely for  $PGV < 5$  mm/s. For vulnerable buildings, the associated vibration level is 3 mm/s. Human perceptibility is expected to start at 0.3-0.5 mm/s.

### 8.3.3 Magnitude Thresholds

Measured ground vibrations related to the largest magnitude  $M_L=1.7$  earthquake yield a peak value of  $PGV=1.1$  mm/s. We use this value in combination with the definition of the Richter magnitude to estimate a magnitude threshold of  $M_L \geq 1.4$  at which an earthquake occurring at the same location can be felt (i.e. causing  $PGV \geq 0.5$  mm/s). The magnitude level at which damage to ordinary buildings is considered possible (i.e.  $PGV \geq 5$  mm/s) is estimated at  $M_L \geq 2.4$  for an earthquake occurring at the same location.

### 8.3.4 Mitigation Measures




Although not expected, the occurrence of induced seismicity in a future production scenario cannot be ruled out. Acknowledging for uncertainties of subsurface conditions, several scenarios are conceivable where future geothermal production could cause seismicity as outlined in section 8.3.1.

To prevent the occurrence of larger magnitude earthquakes, a widely used risk mitigation measure is the traffic light system (TLS, compare chapter 5), where operations are interrupted if the strength of reservoir seismicity exceeds pre-defined threshold values.

For future operation of the CLG doublet we suggest operating a TLS as outlined in *Table 6*. Threshold values are designed such that operations are stopped if an earthquake occurs at the lowest level at which human perceptibility is deemed possible (section 8.3.2). The vibration amplitude of the red light threshold is by an order of magnitude smaller than the amplitude level at which material damage starts to become possible (section 8.3.2).

The safety margin between the TLS red threshold and the onset of material damage is proposed to account for trailing effects where larger magnitude events could occur post-operation (compare chapter 5). On the Richter magnitude scale, the proposed safety margin corresponds to 1.3 magnitude units  $M_L$ , i.e. operations are stopped if an earthquake occurs exhibiting a magnitude which is 1.3  $M_L$  units smaller than the magnitude level at which material damage to ordinary buildings is deemed possible. Although a TLS may not work with arbitrary precision (compare Baisch et al., 2019), observations from other geothermal doublets operated in active Graben systems (i.e. Landau, Insheim, Soultz-sous-Forets, Rittershoffen) do not indicate the occurrence of uncontrollable magnitude escalation.

The operation of a TLS requires a seismic station network for monitoring the entire region subjected to stress perturbations in (near-) real-time. The lower detection level of the seismic monitoring system currently operated at Californië (Appendix A) is considered to be sufficient for operating the proposed TLS.

<b>TLS Status</b>			
<b>Definition</b>	PGV < 0.1 mm/s	PGV ≥ 0.1 mm/s	PGV ≥ 0.3 mm/s
<b>Actions</b>	none	<ol style="list-style-type: none"> <li>investigate likely cause and potential mitigation measures</li> <li>report to regulator</li> </ol>	<ol style="list-style-type: none"> <li>stop operations</li> <li>report immediately to regulator</li> </ol>

*Table 6: Definition of TLS threshold values. The TLS applies to all earthquakes whose epicenters are located within 5 km to a reference point centered at (N51.4265° / E6.0886°). Hypocentral depth is not included in the TLS criteria due to its strong dependency on the assumed seismic velocity model. Peak ground velocities (PGV) refer to the vertical seismic moment component.*

## 8.4 Qualitative Risk Assessment

A qualitative risk assessment is performed following the methodology outlined in the recommendations for seismic hazard assessment of geothermal systems in The Netherlands (Baisch et al., 2016).

As discussed in section 8.3.1, induced seismicity is not expected to occur on the known faults. For the risk assessment we consider the hypothetical case of an undetected, critically stressed fault. We do not assume any magnitude limit resulting from the geometry of the hypothetical fault. In this case the maximum possible earthquake magnitude on the hypothetical fault is solely determined by the efficiency of the TLS.

The proposed TLS (section 8.3.4) is designed to prevent the occurrence of material damage even when accounting for a trailing effect of 1.3 magnitude units ( $M_L$ ). Observations from previous seismicity indicate that the TLS red threshold corresponds to a reservoir earthquake of  $M_L=1.1$  and material damage to ordinary buildings cannot be excluded for  $M_L \geq 2.4$  (section 8.3.3). We associate an  $M_L=2.4$  reservoir earthquake with moderate consequences following the scheme proposed by Baisch et al. (2016).

Assuming Gutenberg-Richter statistics (with  $b=1$ ), the occurrence probability of an  $M_L=2.4$  reservoir earthquake is <10% conditional to the previous occurrence of an  $M_L=1.1$ . It should be noted, however, that the absolute occurrence probability of an  $M_L=2.4$  earthquake can be orders of magnitude smaller and cannot be predicted. We qualitatively rank the occurrence

probability in between unlikely and credible. Figure 22 shows the resulting risk matrix.

		Probability of occurrence				
		rare	unlikely	credible	probable	likely
Severity of consequences	negligible					
	minor					
	moderate			●		
	significant					
	severe					

Figure 22: Qualitative risk matrix for the future production scenario of the CLG doublet with the proposed TLS. See text for details.

### 9 RECOMMENDATIONS

The seismic hazard assessment conducted in the current study concludes that resuming geothermal production with the CLG doublet (with production rate of 200m<sup>3</sup>/h) will most likely not cause seismicity on the known faults. A TLS is proposed for limiting the strength of earthquakes potentially occurring on an unmapped fault.

With the proposed TLS the remaining seismic risk associated with resuming CLG production is considered to be acceptable.

These conclusions are based on a deterministic analysis of the stress changes associated with previous and future geothermal production. Although our geomechanical interpretation provides a plausible explanation for the occurrence of previous seismicity, uncertainties remain regarding subsurface structures and the level of stress changes at which earthquakes were triggered at Californië. This is especially true for the  $M_L=0$  event #8 (Table 1) for which the triggering cause remains unclear.

Therefore, we recommend reviewing the concept and assumptions of the current study in case any seismic event (regardless of magnitude) occurs during future production of the CLG doublet. In particular we recommend stopping production if an earthquake occurs in the vicinity of the previous cluster of seismic activity near the CWG injector. Such an earthquake could indicate that earthquakes can be triggered at a lower stress perturbation level than considered in the current study.

## REFERENCES

- Abdullah, R. A., 2006. A study on stress-strain behaviour of granite and sandstone using closed-circuit servo-controlled testing machine, Master thesis, Universiti Teknologi Malaysia.
- Akkar. S., Sandikkaya, M.A., and J.J. Bommer, 2013, Empirical ground-motion models for point- and extended-source crustal earthquake scenarios in Europe and the Middle East, *Bulletin of Earthquake Engineering*, published online: 31 May 2013, doi: 10.1007/s10518-013-9461-4.
- Baisch, S., and H.-P.Harjes, 2003. A model for fluid injection induced seismicity at the KTB. *Geophys. Jour. Int.*, **152**, 160-170.
- Baisch, S., Weidler, R., Vörös, R., and R. Jung, 2006. A conceptual model for post-injection seismicity at Soultz-sous-Forêts. *Geothermal Resources Council, Trans.*, **30**, 601-606.
- Baisch, S., Vörös, R., Weidler, R., and D., Wyborn, 2009. Investigation of Fault Mechanisms during Geothermal Reservoir Stimulation Experiments in the Cooper Basin (Australia). *Bull. Seism. Soc. Amer.*, **99**(1), 148-158.
- Baisch, S., Vörös, R., Rothert, E., Stang, H., Jung, R., and R. Schellschmidt, 2010. A numerical model for fluid injection induced seismicity at Soultz-sous-Forêts. *Int. Jour. Rock Mech. Min. Sci.*, **47**, 405-413.
- Baisch, S., Rothert, E., Stang, H., Vörös, R., Koch, C., and A. McMahon, 2015. Continued geothermal reservoir stimulation experiments in the Cooper Basin (Australia). *Bull. Seism. Soc. Amer.*, **105**, 198-209.
- Baisch, S., Koch, C., Stang, H., Pittens, B., Drijver, B., and N. Buik, 2016. Defining the Framework for Seismic Hazard Assessment in Geothermal Projects V0.1. Technical Report prepared for Dutch Geothermal Research Agenda, vers. 160915, 65 pages.
- Baisch, S., Koch, C., and A. Muntendam-Bos, 2019. Traffic Light Systems: To What Extent Can Induced Seismicity Be Controlled?. *Seismol. Res. Lett.*, in press.
- Baisch, S. and R. Vörös, 2019. Interpretation of the Earthquakes Near the Californië Geothermal Site: August 2015 – November 2018. Report CLGG005\_190207, Q-con GmbH.
- Baria, R., Michelet, S., Baumgärtner, J., Byer, B., Gerard, A., Nicholls, J., Hettkamp, T., Teza, D., Soma, N. Asanuma, H., Garnish, J., and T. Megel, 2004. Microseismic monitoring of the world's largest potential HDR reservoir. *Proceedings, 29th Workshop on Geothermal Reservoir Engineering*, Stanford University, Stanford, California, January 26-28, 2004.

- Berg, M.W. van den, 1994. Neotectonics of the Roer Valley rift system. Style and rate of crustal deformation inferred from syn-tectonic sedimentation. *Geologie en Mijnbouw*, **73**, 143-156.
- Bommer, J. J., Oates, S., Cepeda, J. M., Lindholm, C., Bird, J., Torres, R., Marroquin, G., and J. Rivas, 2006. Control of hazard due to seismicity induced by a hot fractured rock geothermal project. *Eng. Geol.*, **83**, 287-306.
- Bönnemann, C., Schmidt, B., Ritter, J., Gestermann, N., Plenefisch, T. and U. Wegler, 2010. Das seismische Ereignis bei Landau. Abschlussbericht der Expertengruppe „Seismisches Risiko bei hydrothermalen Geothermie, 54 Seiten.
- Buness, H. A., 2004. GeneSys: Ein Beobachtungsnetz für induzierte mikroseismische Ereignisse. Interner Bericht des Instituts f. Geowissenschaftliche Gemeinschaftsaufgaben, Hannover (jetzt LIAG).
- Camelbeeck, T., van Eck, T., Pelzing, R., Ahorner, L., Loohuis, J., Haak, H. W., Hoang-Trong, P., and D. Hollnack, 1994. The 1992 Roermond earthquake, the Netherlands, and its aftershocks, *Geol. Mijnbouw*, **73**, 181–197.
- Costain, J. K., and G. A. Bollinger, 2010. Review: Research results in hydroseismicity from 1987 to 2009. *Bull. Seism. Soc. Amer.*, **100**(5), 1841-1858.
- Dost, B., Van Eck, T., and H. W. Haak, 2004. Scaling of peak ground acceleration and peak ground velocity recorded in the Netherlands. *Bol. Geof. Teo. Appl.*, **45**, 153-168.
- Dost, B., and H. W. Haak, 2007. Natural and induced seismicity. *Geology of the Netherlands*. Edited by Th.E. Wong, D.A.J. Batjes & J. de Jager, Royal Netherlands Academy of Arts and Sciences, 223-239.
- Evans, K., Zappone, A., Kraft, T., Deichmann, N., and F. Moia, 2011. A survey of the induced seismic responses to fluid injection in geothermal and CO<sub>2</sub> reservoirs in Europe, *Geothermics*.
- Hanks, T. C., and H. Kanamori, 1979. A moment magnitude scale, *Jour. Geophys. Res.*, **84**, 2348-2350.
- Healy, J. H., Hamilton, R. M., and C. B. Raleigh, 1970. Earthquakes induced by fluid injection and explosion, *Tectonophysics*, **9**, 205-214.
- Hill, D. P., 2008. Dynamic Stresses, Coulomb Failure, and Remote Triggering, *Bull. Seism. Soc. Amer.*, **98**(1), 66-92.
- Hinzen, K. G., 2003. Stress field in the Northern Rhine area, Central Europe, from earthquake fault plane solutions. *Tectonophysics*, **377**, 325-356.
- Houtgast, R.F., and R.T. van Balen, 2000. Neotectonics of the Roer Valley Rift System, the Netherlands., *Global and Planetary Change*, **27**, 131-146.
- Hsieh, P. A., and J. D. Bredehoeft, 1981. A reservoir analysis of the Denver earthquakes: A



- case of induced seismicity, *Jour. Geophys. Res.*, **86**, 903-920.
- Husen, S., Bachmann, C., and D. Giardini, 2007. Locally triggered seismicity in the central Swiss Alps following the large rainfall event of August 2005. *Geophys. J. Int.*, doi: 10.1111/j.1365-246X.2007.03561.x.
- Keranen, K. M., Weingarten, M., Alters, G. A., Bekins, B. A., and S. Ge, 2014. Sharp increase in central Oklahoma seismicity since 2008 induced by massive wastewater injection. *Science*, **345** (6195), 448-451.
- Kim, K.-H., Ree, J.-H., Kim, Y., Kim, S., Kang, S. Y., and W. Seo, 2018. Assessing whether the 2017  $M_w$ 5.4 Pohang earthquake in South Korea was an induced event. *Science*, 10.1126/science.aat6081.
- Küperkoch, L., Olbert, K., and T. Meier, 2018. Long-Term Monitoring of Induced Seismicity at the Insheim Geothermal Site, Germany. *Bull. Seism. Soc. Amer.*, **108**, 10.1785/0120170365.
- Kwiatek, G., Bohnhoff, M., Dresen, G., Schulze, A., Schulte, T., Zimmermann, G., and E. Huenges, 2010. Microseismicity induced during fluid-injection: A case study from the geothermal site at Groß Schönebeck, North German Basin. *Acta Geophysica*, **58**(6), p. 995-1020.
- Megies, T., and J. Wassermann, 2014. Microseismicity observed at a non-pressure-stimulated geothermal power plant. *Geothermics*, doi:10.1016/j.geothermics.2014.01.002.
- Miller, S. A., 2008. Note on rain-triggered earthquakes and their dependence on karst geology. *Geophys. J. Int.*, doi:10.1111/j.1365-246X.2008.03735.x.
- National Academy of Science (NAS), 2013. Induced Seismicity Potential in Energy Technologies. National Research Council report, Washington, DC: The National Academic Press.
- Okada, Y., 1992. Internal Deformation due to Shear and Tensile Faults in a Half-Space. *Bull. Seism. Soc. Amer.*, **82**, 1018-1040.
- Plenefisch, T., Bonjer, K.-P., 1997. The stress field in the Rhine Graben area inferred from earthquake focal mechanisms and estimation of frictional parameter. *Tectonophysics*, **275**, 71-97.
- Stang, H., and E. Rothert, 2014. Geothermal Project Californië - Installation & Commissioning - Seismic Monitoring Stations. Q-con report WSC001 prepared for GeoWeb BV, version 140903, 16 pages.
- Rothert, E., and H. Stang, 2015. Geothermal Project Californië - Extended Seismic Monitoring Network – Noise Measurements & Detection Threshold. Q-con report CLGG003 prepared for CLG, version 151201, 28 pages.

- SBR, 2010. Schade aan Gebouwen, Deel A uit de Meet- en beoordelingsrichtlijn: Trillingen.
- Schoenball, M., Rall Walsh, F., Weingarten, M., and W. L. Ellsworth, 2018. How faults wake up: The Guthrie-Langston, Oklahoma earthquakes. *The Leading Edge*, **37**, 810-816.
- Scholz, C. H., 2002. The Mechanics of Earthquakes and Faulting, Cambridge University Press, 2<sup>nd</sup> Edition.
- VITO, 2010. 2D Seismische Campagne Californie. Confidential VITO report prepared for Grondexploitatie maatschappij Californië BV en Tuinbouwbedrijf Wijnen BV, EINDRAPPORT, 2010/SCT/R/033, Februar 2010, 33 pages.
- VITO, 2018. Updated reservoir model provided to Q-con by E-mail, 29.3.2018.
- Vörös, R., Baisch, S., and H. Stang, 2015. Seismic Hazard Assessment for the Extended Geothermal System Californie. Report CLG001\_150831, Q-con GmbH.
- Worum, G., van Wees, J.-D., Bada, G., van Balen, R. T., Cloetingh, S., and H. Pagnier, 2004. Slip tendency analysis as a tool to constrain fault reactivation: A numerical approach applied to three-dimensional fault models in the Roer Valley rift system (southeast Netherlands), *J. Geophys. Res.*, **109**(B02401), 1-16.
- Yamaji, A., 2007. An Introduction to Tectonophysics. *Terrapub*.
- Zoback, M. D., Barton, C. A., Brudy, M., Castillo, D. A., Finkbeiner, T., Grollmund, B. R., Moos, D. B., Peska, P., Ward, C. D., and D. J. Wiprut, 2003. Determination of stress orientation and magnitude in deep wells. *Int. Jour. Rock Mech. Min. Sci.*, **40**, 1049-1076.

## APPENDIX A SEISMIC STATION NETWORK

A permanent seismic monitoring system with three seismometer stations was deployed in August 2014 to monitor operations of the CWG doublet (Stang & Rothert, 2014). Two additional seismometer stations were deployed in November 2015 to monitor the extended geothermal system Californië (Rothert & Stang, 2015). The average 195 noise level at the five seismometer stations varies between 0.001 mm/s and 0.006 mm/s (Rothert & Stang, 2015). Figure 23 shows the lower magnitude detection threshold of the seismic network as simulated by Rothert & Stang (2015). Simulation results indicate that the monitoring network robustly detects reservoir earthquakes with  $M_w \geq 0.4$  occurring within 3-4 km of the geothermal sites.

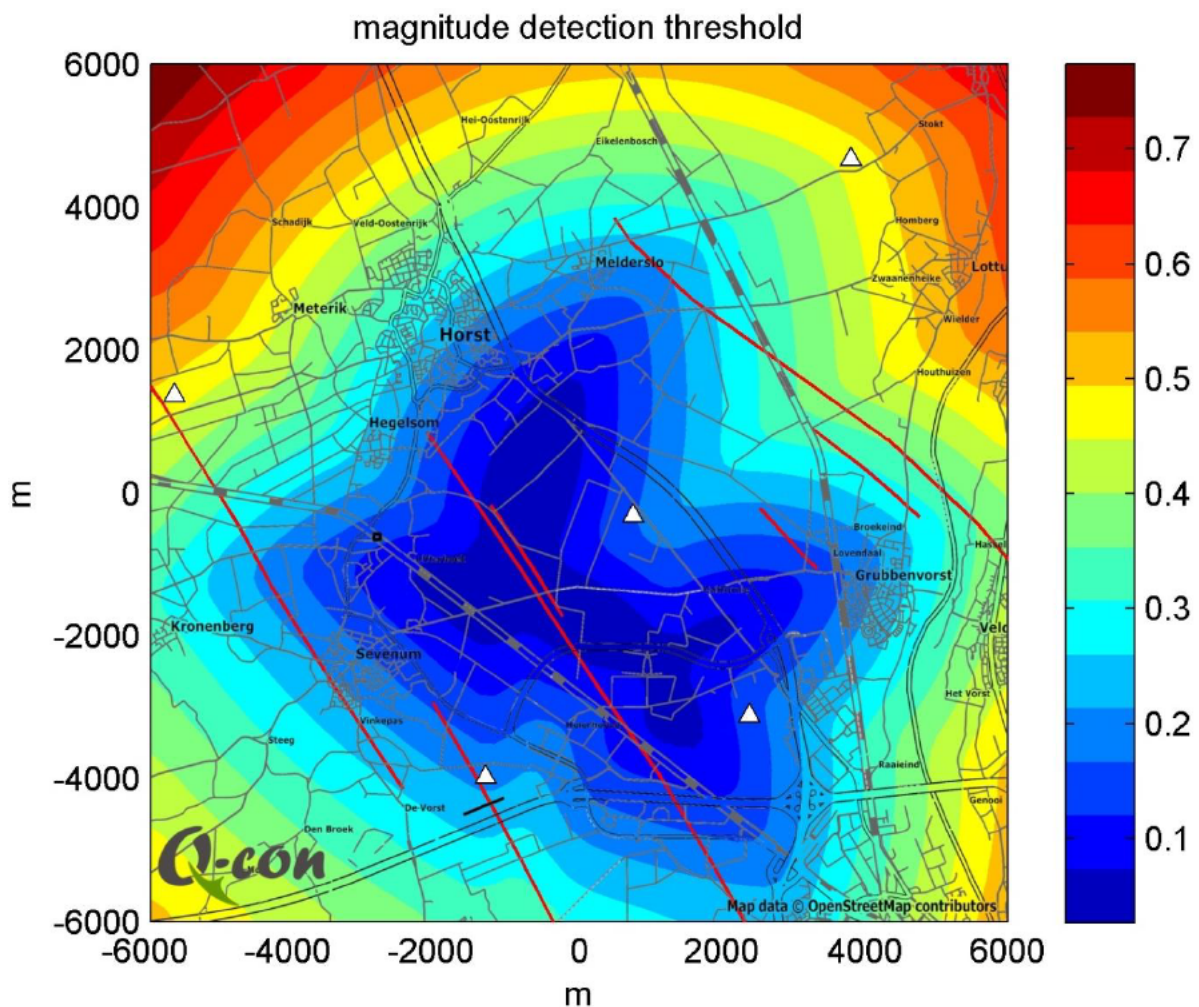


Figure 23: Simulated lower magnitude detection threshold  $M_w$  for seismicity occurring at reservoir depth according to the color scale. The five stations of the seismic network are depicted by white triangles. Red lines denote the trajectories of the mapped faults at reservoir level. Coordinate system centered at the CLG injection well GT05. Figure from Rothert & Stang (2015).

## APPENDIX B ADDITIONAL NUMERICAL SIMULATIONS

### B.1. Fluid Pressure

To account for uncertainties associated with the assumed boundary conditions, two end-member scenarios are considered.

#### **No flow boundaries**

In the first simulation, all lateral model boundaries are set to 'no flow'. Figure 24 shows the simulated hydraulic pressure distribution during the simultaneous simulation of both doublets with maximum flow rates in January 2018. Consistent with observations, the overpressure at the GT05 injection well exceeds 30 bars. Overpressure at the Velden fault is in the order of 5 bars. This pressure level is to some extent depending on the hydraulic properties of the Velden fault. In the extreme case of a sealing fault, the spatial extension of the numerical model is effectively reduced towards the East. In this case, the level of overpressure in the immediate vicinity of the Velden fault is slightly higher than shown in *Figure 20*, while stationary conditions are approximately reached at the same time. It should be noted, however, that the pressure inside a sealing fault is not affected by geothermal activities.

Alternatively, a highly conductive Velden fault leads to faster pressure leveling compared to *Figure 20*. Most relevant for the current hazard assessment is the conclusion that quasi-stationary pressure conditions were already reached during previous CLG production. This conclusion is independent of the assumed properties of the Velden fault.

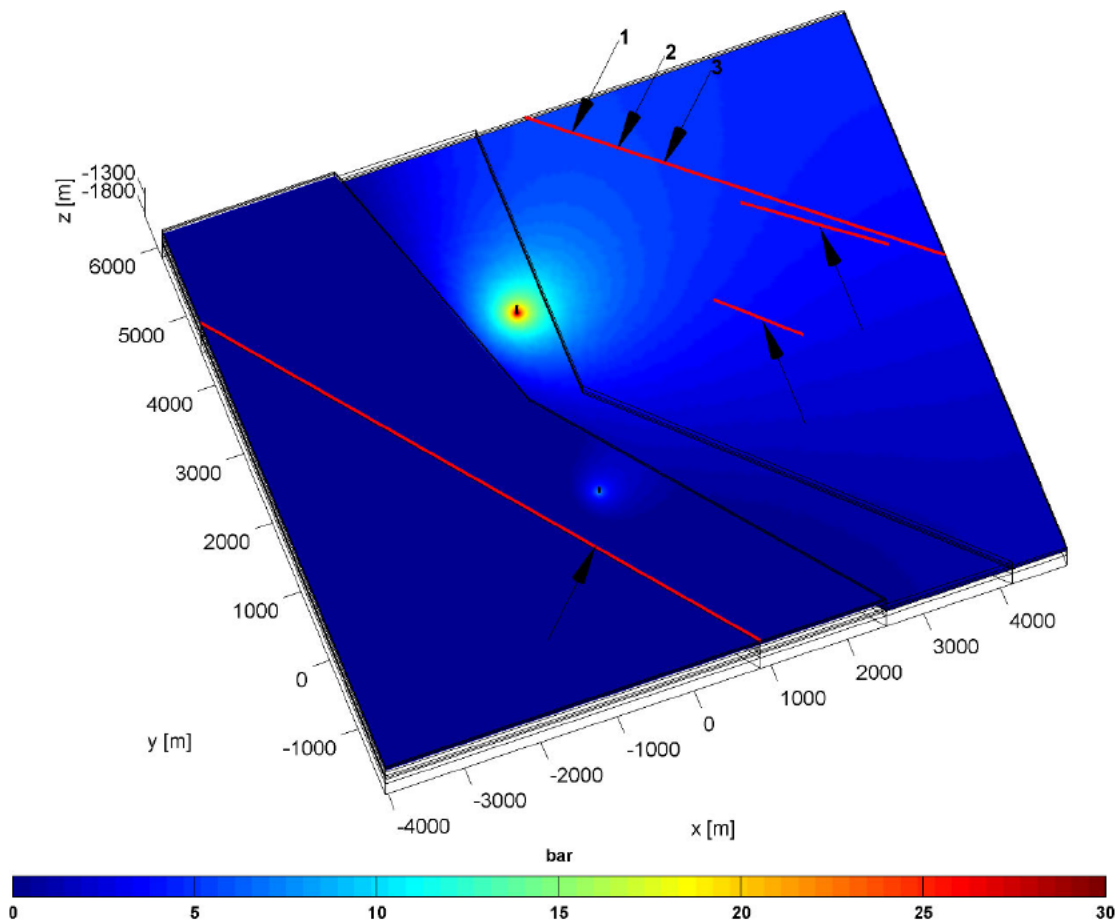


Figure 24: Simulated pressure distribution in mid-January 2018. Hydraulic pressure is indicated in bar according to the colormap. Arrows point to locations on the faults which are referred to in the text (hydraulic pressure samples). Consistent with observations (Figure 14), the overpressure at the GT05 injection well exceeds 30 bars. The overpressure at the GT03 injection well is comparatively smaller and shows up in the vicinity of the injection well only (light blue colors). Due to the high transmissivity of the Tegelen fault, the pressure drawdown at the production wells is small and is less localized.

### Constant pressure boundaries

The numerical simulations are repeated, setting all lateral model boundaries to 'constant pressure'. Since the Velden fault is located close to model boundaries, it is clear that the absolute pressure level on the Velden fault is dominated by the assumed boundary conditions. Therefore, the absolute pressure level on the Velden fault should not be interpreted. The simulation solely aims to demonstrate that quasi-stationary conditions tend to be reached earlier due to the presence of zero-pressure boundaries while the level of overpressure is generally reduced. This is shown in Figure 25 where quasi-stationary conditions are reached already by mid-October 2017.

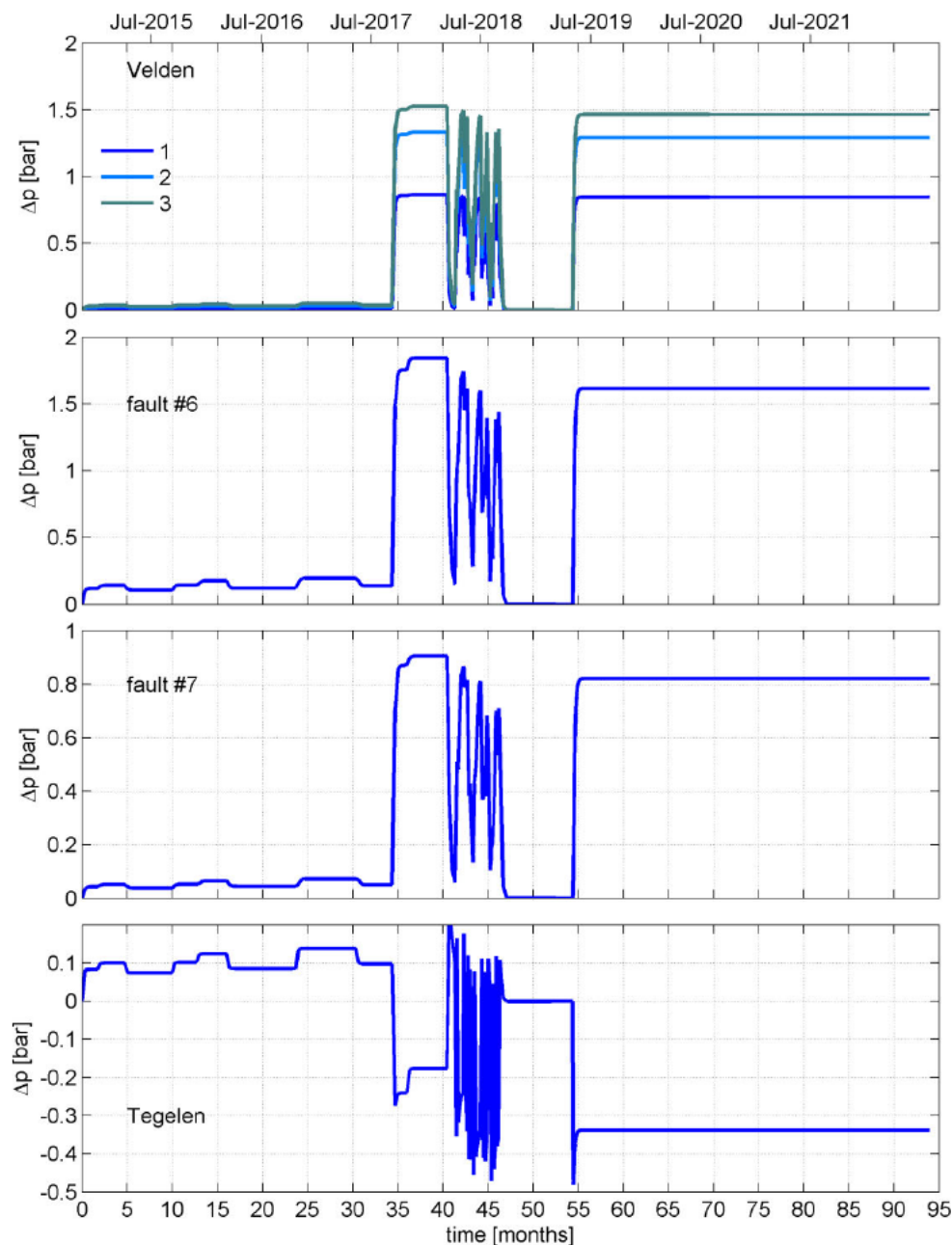


Figure 25: Temporal evolution of numerically simulated hydraulic pressure during previous geothermal production and for future production of the CLG doublet at the mapped faults. Constant pressure model boundaries were assumed. Average CLG flow rates were used as indicated in Figure 14. The initial CLG testing phase with strong variations of production rate was deliberately ignored. Ignoring the initial testing phase implies that actual quasi-stationary conditions tend to be reached later with the current simulations (conservative perspective). Future production has been simulated for 20 years but is shown for 3 years only as the pressure level reached its maximum already after a few months time. Geothermal production reduced the pore pressure on the Tegelen by 0.3 bars. After production stop, pore pressure slowly returns to its original (virgin) level.

## B.2. Thermal Reservoir Contraction

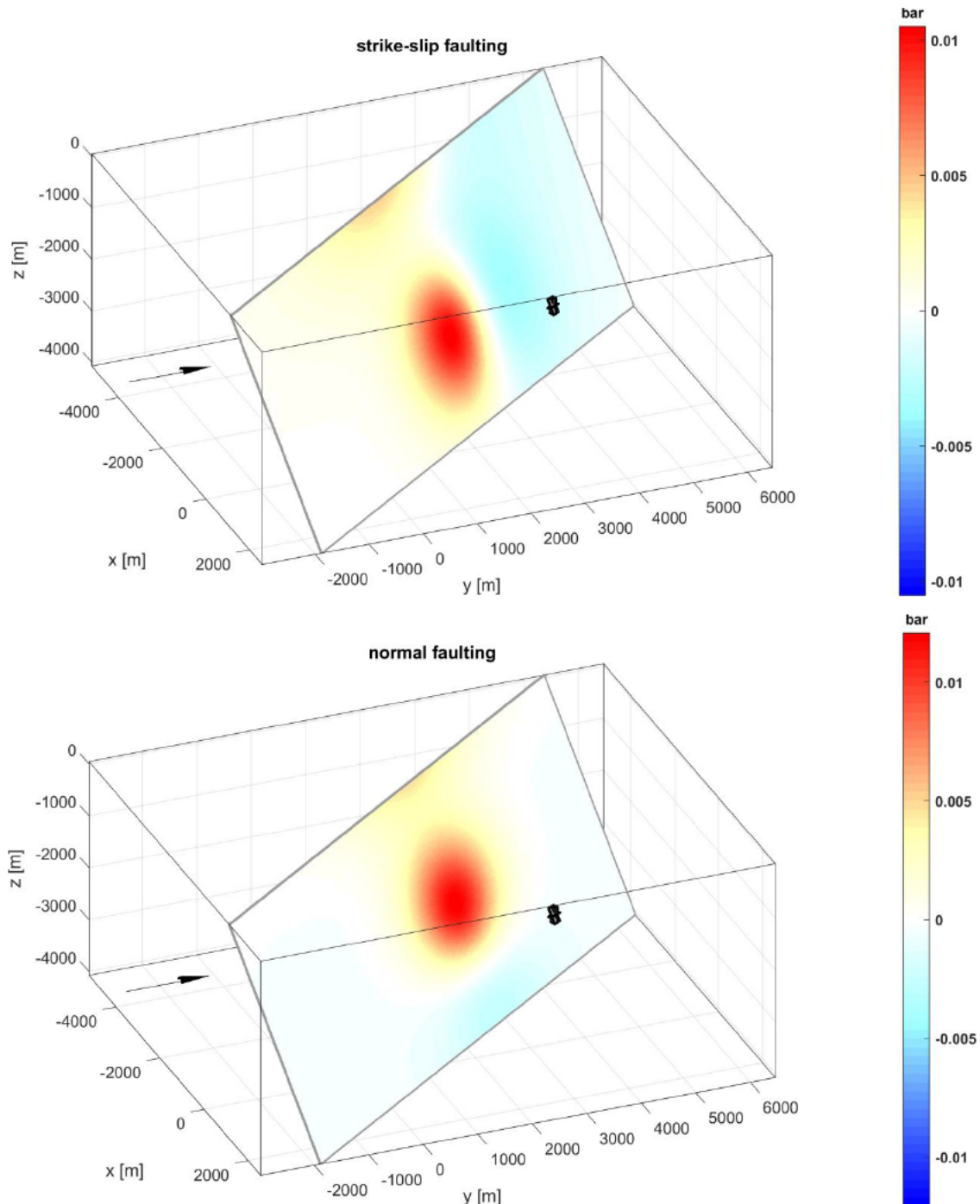


Figure 26: Simulated Coulomb stress changes on the Tegelen fault related to previous geothermal production with the CLG doublet. Stress magnitudes in bar according to color scale (range defined by maximum values). Stress perturbations assuming left lateral strike slip failure (top) and normal faulting (bottom). The contraction source (orthogonal Okada sources representing the contracted reservoir rock) is depicted as grey planes. Black arrow denotes Northern direction.

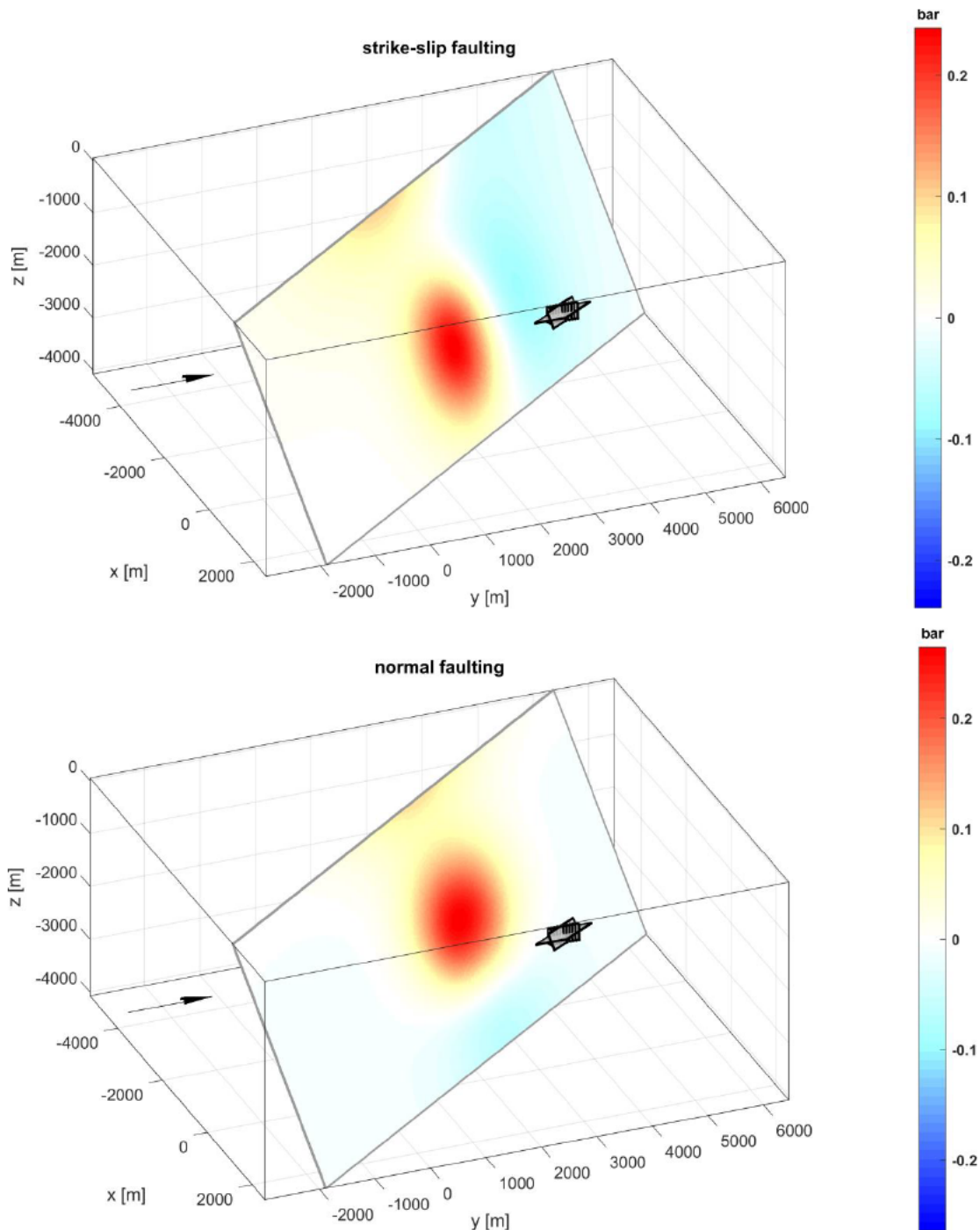


Figure 27: Simulated Coulomb stress changes on the Tegelen fault after 20 years of future CLG production. Stress magnitude in bar according to color scale (range defined by maximum values). Stress perturbations assuming left lateral strike slip failure (top) and normal faulting (bottom). The contraction source (orthogonal Okada sources representing the contracted reservoir rock) is depicted as grey planes. Black arrow denotes Northern direction.



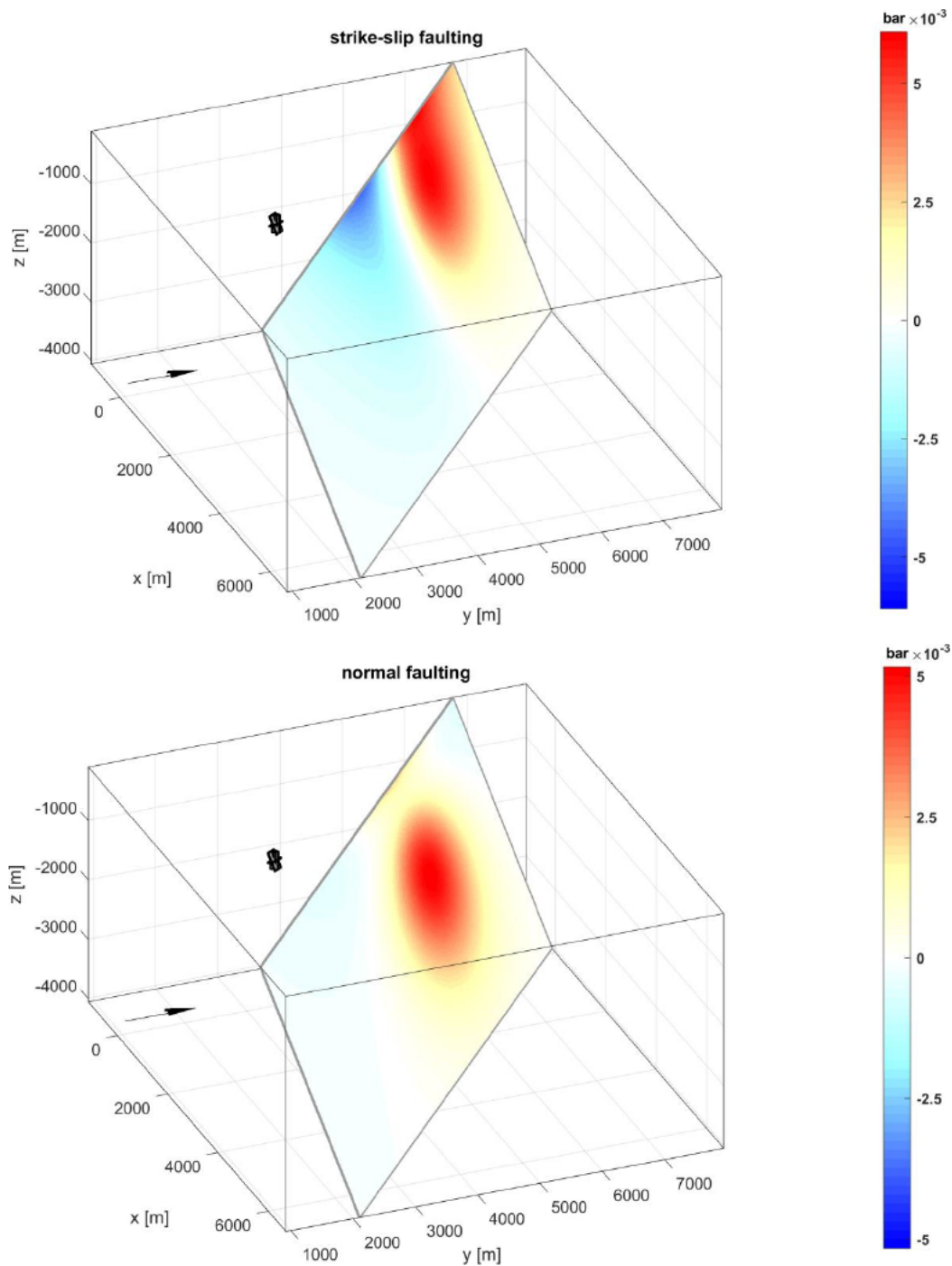


Figure 28: Simulated Coulomb stress changes on the Velden fault related to previous geothermal production with the CLG doublet. Stress magnitude in bar according to color scale (range defined by maximum values). Stress perturbations assuming left lateral strike slip failure (top) and normal faulting (bottom). The contraction source (orthogonal Okada sources representing the contracted reservoir rock) is depicted as grey planes. Black arrow denotes Northern direction.

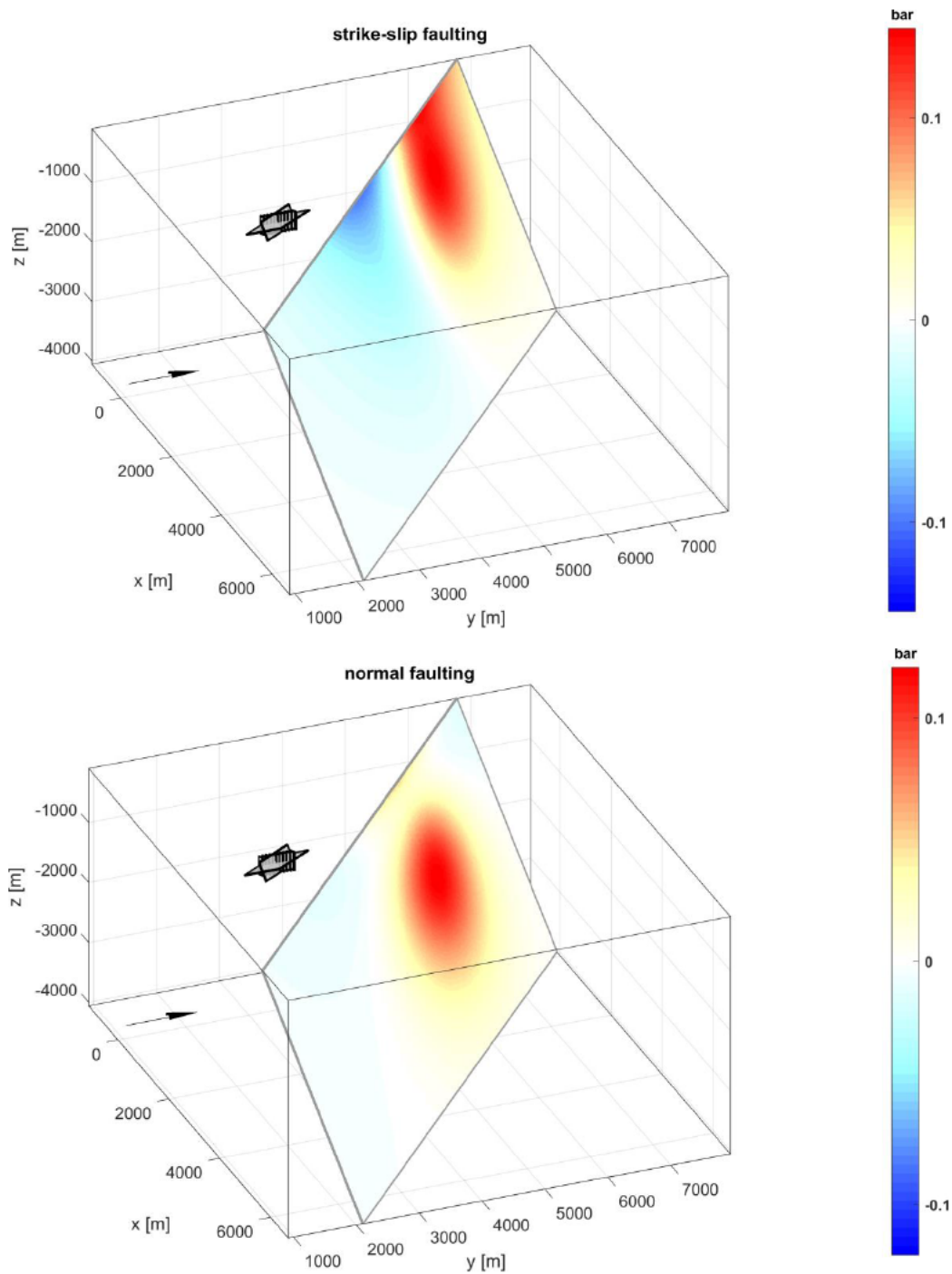


Figure 29: Simulated Coulomb stress changes on the Velden fault after 20 years of future CLG production. Stress magnitude in bar according to color scale (range defined by maximum values). Stress perturbations assuming left lateral strike slip failure (top) and normal faulting (bottom). The contraction source (orthogonal Okada sources representing the contracted reservoir rock) is depicted as grey planes. Black arrow denotes Northern direction.

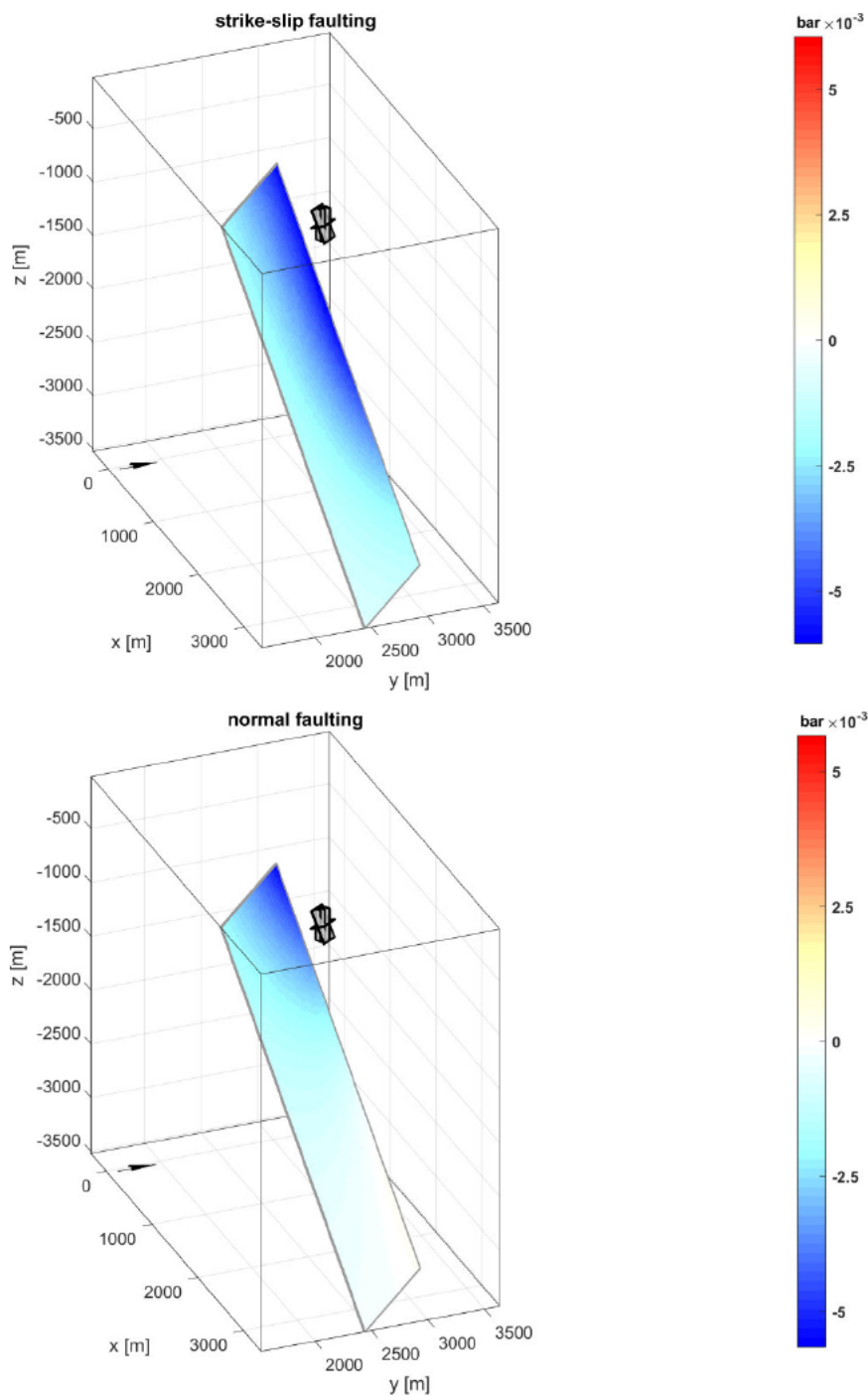


Figure 30: Simulated Coulomb stress changes on fault#6 related to previous geothermal production with the CLG doublet. Stress magnitude in bar according to color scale (range defined by maximum values). Stress perturbations assuming left lateral strike slip failure (top) and normal faulting (bottom). The contraction source (orthogonal Okada sources representing the contracted reservoir rock) is depicted as grey planes. Black arrow denotes Northern direction.

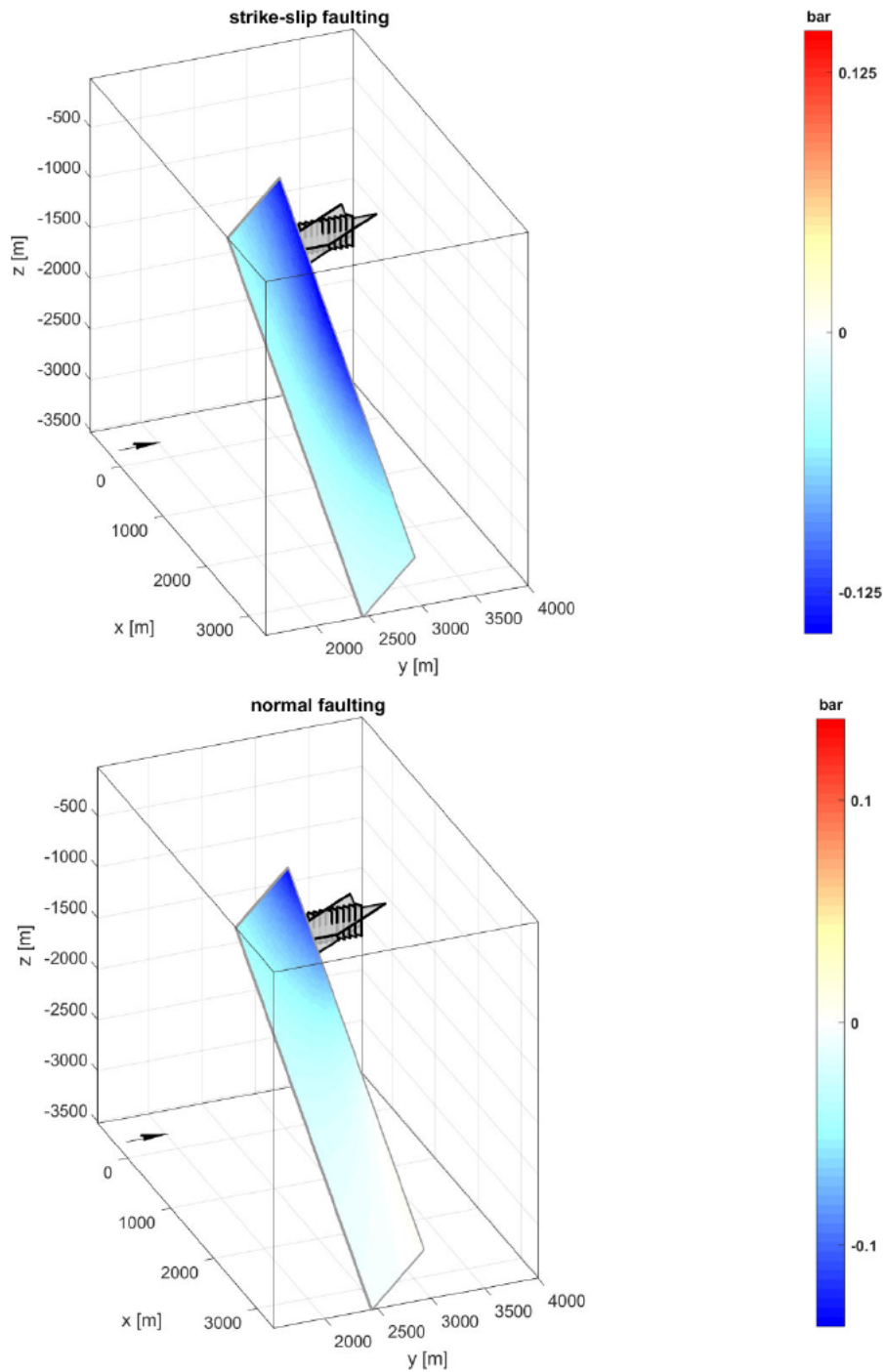


Figure 31: Simulated Coulomb stress changes on fault#6 after 20 years of future CLG production. Stress magnitude in bar according to color scale (range defined by maximum values). Stress perturbations assuming left lateral strike slip failure (top) and normal faulting (bottom). The contraction source (orthogonal Okada sources representing the contracted reservoir rock) is depicted as grey planes. Black arrow denotes Northern direction.

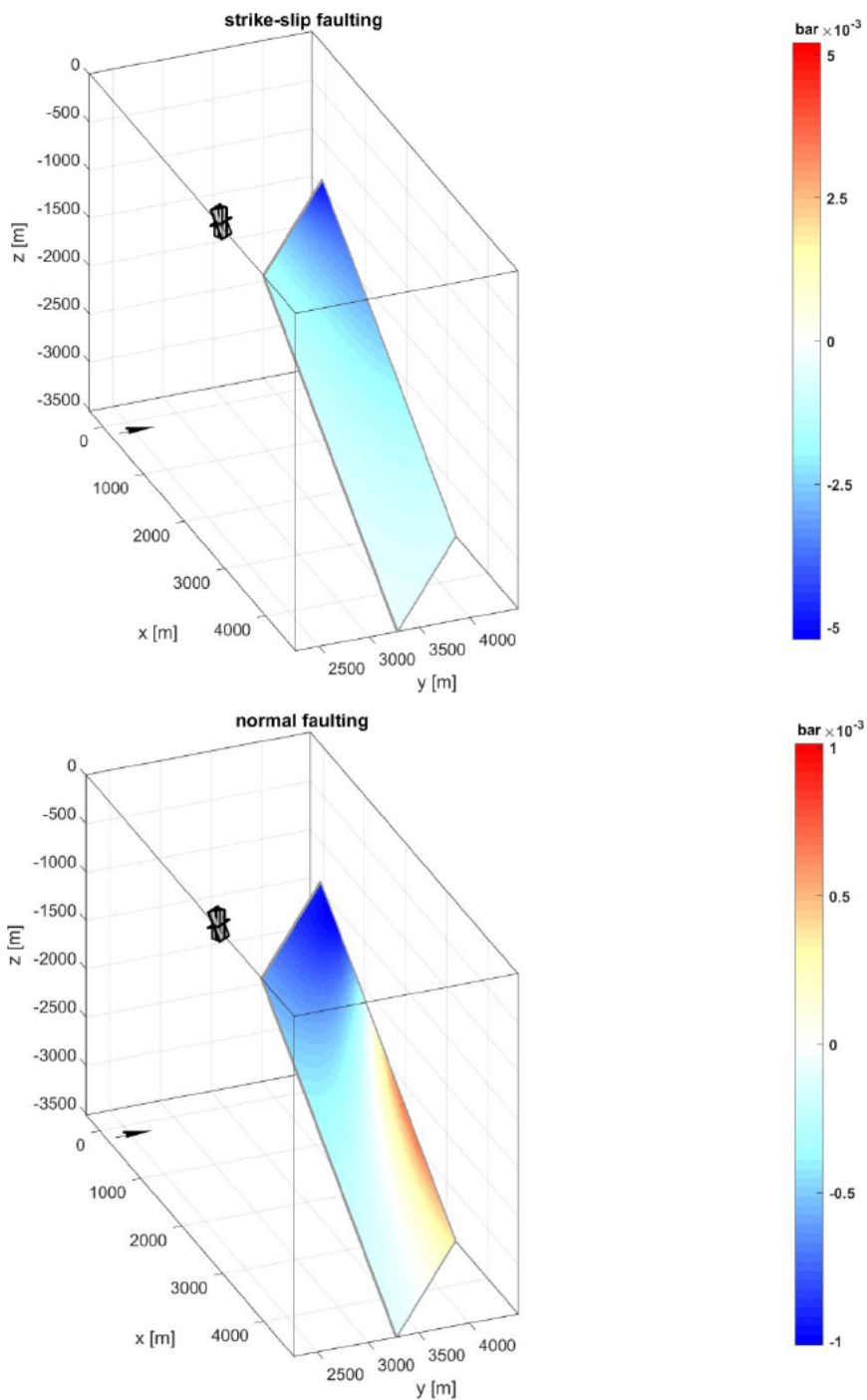


Figure 32: Simulated Coulomb stress changes on fault#7 related to previous geothermal production with the CLG doublet. Stress magnitude in bar according to color scale (range defined by maximum values). Stress perturbations assuming left lateral strike slip failure (top) and normal faulting (bottom). The contraction source (orthogonal Okada sources representing the contracted reservoir rock) is depicted as grey planes. Black arrow denotes Northern direction.

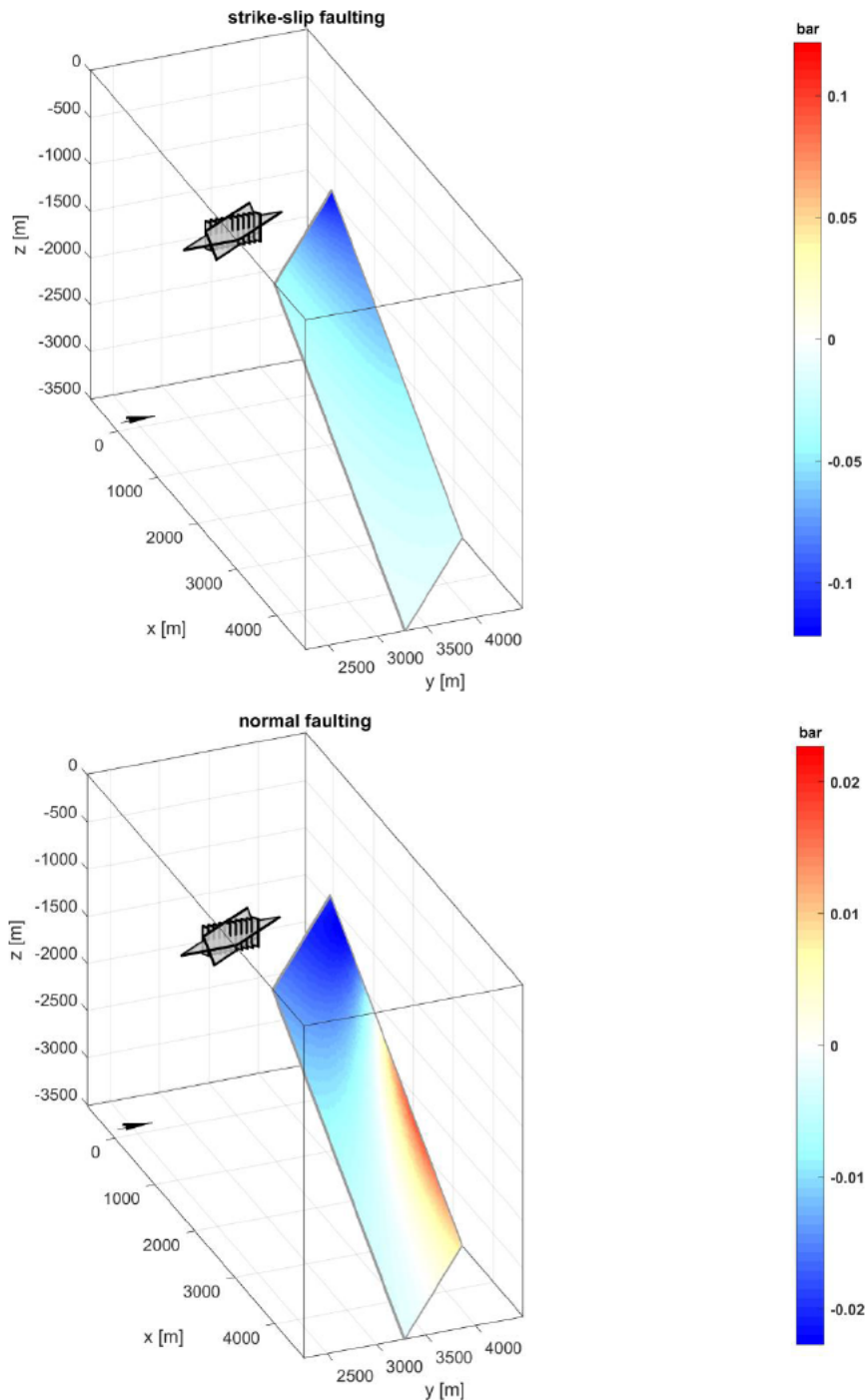


Figure 33: Simulated Coulomb stress changes on fault#7 after 20 years of future CLG production. Stress magnitude in bar according to color scale (range defined by maximum values). Stress perturbations assuming left lateral strike slip failure (top) and normal faulting (bottom). The contraction source (orthogonal Okada sources representing the contracted reservoir rock) is depicted as grey planes. Black arrow denotes Northern direction.

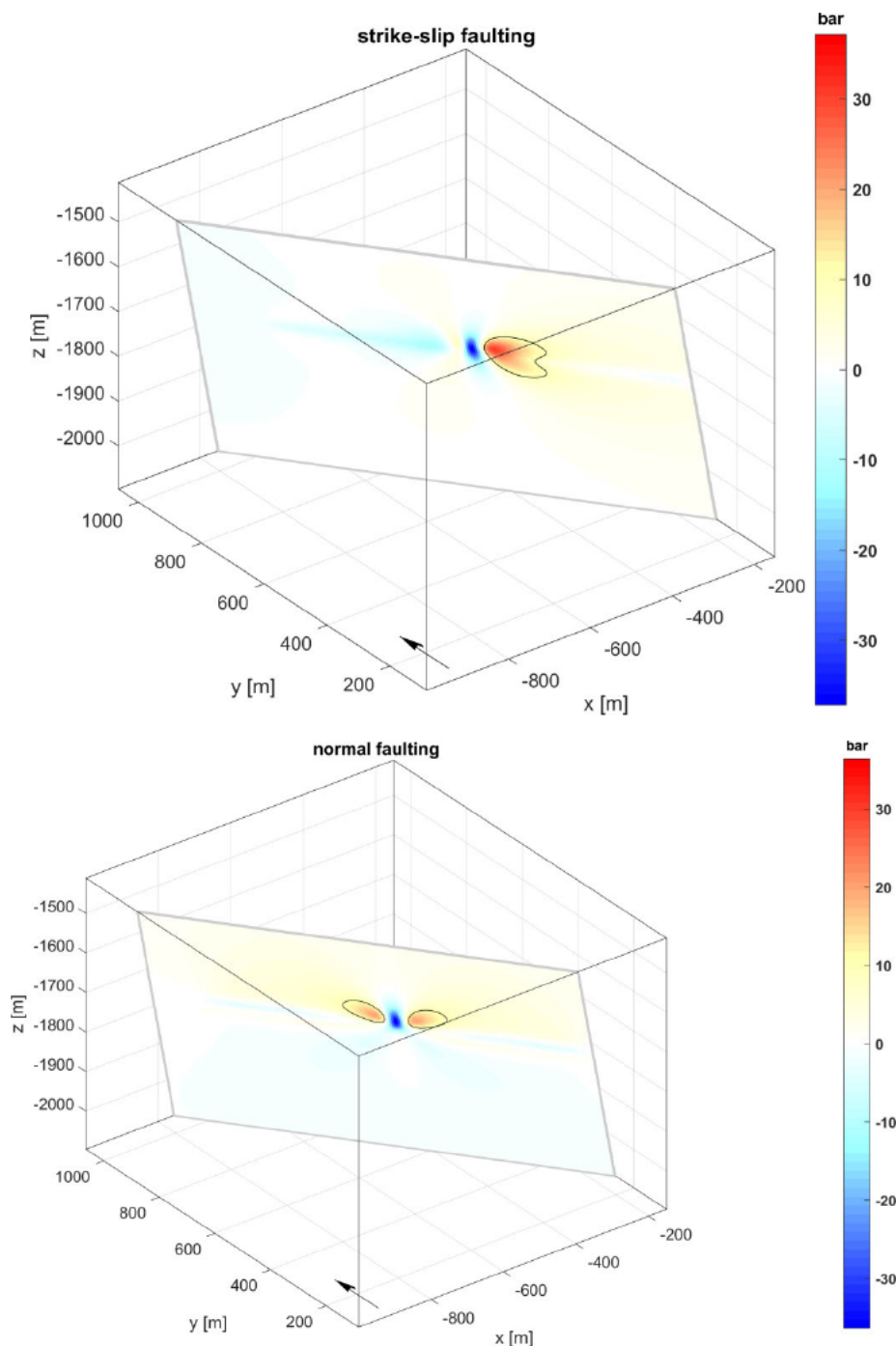


Figure 34: Coulomb stress changes on the Tegelen fault related to previous geothermal production with the CWG doublet. Stress magnitude in bar according to color scale (range defined by maximum values). Stress perturbations assuming left lateral strike slip failure (top) and normal faulting (bottom). Black line outlines area with  $\Delta CS \geq 10$  bars. Note: in addition to previous modelling, a sensitivity analysis was performed to study the impact of the assumed compaction direction. Here we have assumed the orientation of the cooling front in normal direction of the fault and confined the cooling front to the most conductive layer L2 only, which is leading to higher  $\Delta CS$  values compared to previous modelling results (Baisch & Vörös, 2019).